arXiv:2106.09191v3 [math.NA] 26 Oct 2021

The Biot-Stokes coupling using total pressure: formulation, analysis and application to interfacial flow in the eye

Ricardo Ruiz-Baier[a,b,c,*], Matteo Taffetani[d], Hans D. Westermeyer[e], Ivan Yotov[f]

[a] *School of Mathematics, Monash University, 9 Rainforest Walk, Clayton, Victoria 3800, Australia.*

[b] *Institute of Computer Science and Mathematical Modelling, Sechenov University, Moscow, Russian Federation.*

[c] *Universidad Adventista de Chile, Casilla 7-D, Chillán, Chile.*

[d] *Department of Engineering Mathematics, University of Bristol, BS8 1TR Bristol, United Kingdom.*

[e] *Department of Clinical Sciences, College of Veterinary Medicine, North Carolina State University, 1060 William Moore Drive, Raleigh, NC 27607, USA.*

[f] *Department of Mathematics, University of Pittsburgh, Pittsburgh, PA 15260, USA.*

Abstract

We consider a multiphysics model for the flow of Newtonian fluid coupled with Biot consolidation equations through an interface, and incorporating total pressure as an unknown in the poroelastic region. A new mixed-primal finite element scheme is proposed solving for the pairs fluid velocity - pressure and displacement - total poroelastic pressure using Stokes-stable elements, and where the formulation does not require Lagrange multipliers to set up the usual transmission conditions on the interface. The stability and well-posedness of the continuous and semi-discrete problems are analysed in detail. Our numerical study is framed in the context of applicative problems pertaining to heterogeneous geophysical flows and to eye poromechanics. For the latter, we investigate different interfacial flow regimes in Cartesian and axisymmetric coordinates that could eventually help describe early morphologic changes associated with glaucoma development in canine species.

Keywords: Porous media flow, Biot consolidation, total pressure, transmission problem, mixed finite element methods, eye fluid poromechanics.

2000 MSC: 65M60, 65M12, 76S05, 74F10, 92C35.

1. Introduction

Poroelastic structures are found in many applications of industrial and scientific relevance. Examples include the interaction between soft permeable tissue and blood flow, or the study of the spatial growth of biofilm in fluids. When the interaction with a free fluid is considered, the mechanics of the fluid and poroelastic domains are coupled through balance of forces and continuity conditions that adopt diverse forms depending on the expected behaviour in the specific application (see, e.g., [26, 49, 50, 51] and the references therein). The particular problem we consider in this paper as motivation for the

*Author for correspondence. Email: ricardo.ruizbaier@monash.edu. Phone: +61 3 9905 4485.

Email addresses: ricardo.ruizbaier@monash.edu (Ricardo Ruiz-Baier), ho20302@bristol.ac.uk (Matteo Taffetani), hdwester@ncsu.edu (Hans D. Westermeyer), yotov@math.pitt.edu (Ivan Yotov)

design of the finite element formulation is the interfacial flow of aqueous humour between the anterior chamber and the trabecular meshwork (which is a deformable porous structure) in the eye, and how such phenomenon relates to early stages of glaucoma.

Glaucoma encompasses a group of mechanisms that lead to decreased retinal function, impaired visual fields and blindness. The main risk factor for glaucoma in canines is an abnormal increase in the intra-ocular pressure (which under physiologically normal conditions is balanced between aqueous humour production and outflow to the venous drainage system [32]). We are interested in modelling the flow behaviour of aqueous humour within the anterior chamber and its interaction with the poroelastic properties of particular compartments in the drainage outlet located between the base of the iris and the limbus, which, in the dog eye and most other non-primate species consists of an array of thin tissue columns (pectinate ligaments) [46] which mark the boundary of the trabecular meshwork with the anterior chamber. Sketches of the regions of interest are depicted in Figure 1.1. Our focus is on how the physical changes associated with pectinate ligament dysplasia, a change seen in all dogs with primary angle closure glaucoma, affect aqueous humour flow through this boundary. We stress that the ciliary cleft anatomy of all carnivorous mammals is fairly similar to that of the dog. In fact, this anatomy is preserved across much of herbivorous mammals as well (see, e.g., [43]). Therefore, even though the dog is probably the most studied due to its status as a companion animal, this work likely applies to most carnivorous and herbivorous mammals.

The flow within the anterior chamber will be modelled by Navier-Stokes and Stokes' law for Newtonian fluids, whereas the filtration of aqueous humour through the deformable trabecular meshwork and towards the angular aqueous plexus will be described by Darcy's law. Pressure differences are generated by production (from the ciliary muscle) and drainage (to angular aqueous plexus and then linked to the veins at the surface of the sclera through collecting channels) of aqueous humour.

Other effects that could contribute to modification of the flow patterns and that we do not consider here, are thermal properties (buoyancy mechanisms due to temperature gradients from inner to outer cornea) [11], cross-link interaction between fibrils in the cornea [30], pressure changes due to phacodonesis (vibration of the lens while the head or eye itself moves) and Rapid Eye Movement during sleep [29], and nonlinear flow conditions in the filtration region (incorporated in [37] through Darcy-Forchheimer models).

In contrast with [25, 28, 42, 52], here we consider that the coalescing of the pectinate ligaments results in marked changes in porosity properties of the anterior chamber - trabecular meshwork interface, which could eventually lead to progressive collapse of the ciliary cleft. We further postulate that these modifications of the tissue's microstructure could be induced by forces exerted by the flow that concentrate at the interface between the dysplastic pectinate ligament and the anterior chamber, and which occur over a timescale much larger than that of the ocular pulsating flow. In fact, evidence of the compliance of the trabecular meshwork can be found in, e.g., [35]. One of the earliest modelling works including a coupling between aqueous humour in the anterior chamber with complying structures is presented in [33], where mechanical properties of the bovine iris were employed to set an elastic interface to represent blinking. Other fluid-structure interaction models have been recently developed in [54], suggesting that flow conditions in the trabecular meshwork and the outlets could be largely affected by the changes of permeability in microstructure, and [3], where poroelastic properties of the choroid and viscoelastic response of the vitreous body are used to set up a more complete 3D model of larger scale that discards a dedicated physiological description of the trabecular meshwork and considers instead a windkessel model.

In the general context of single phase fluid / poromechanical coupling, there are already a variety

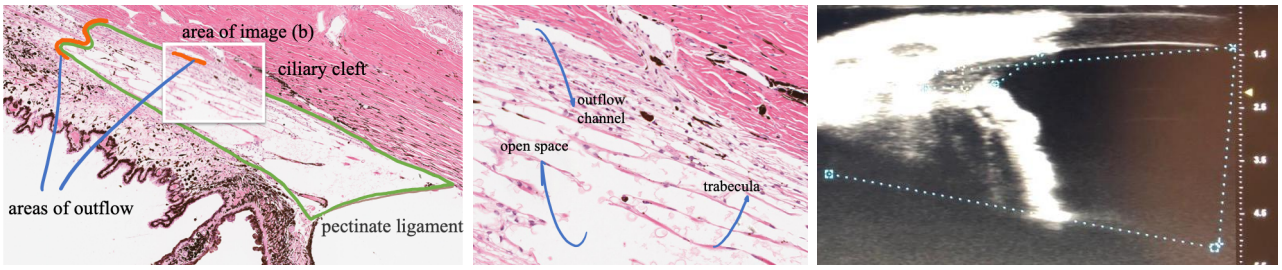

Figure 1.1: Histology sketches of regions of interest (left, centre), and ultrasound image taken from data (right).

of finite element formulations starting from the work [44], which focuses on the effects of secondary consolidation. More recently, partitioned finite element formulations using domain decomposition and or Nitsche's approach for single and double poroelastic layers in contact with a single phase fluid can be found in [9, 16, 17, 39]. Monolithic couplings have been analysed in [7] for a mixed Darcy formulation using a Lagrange multiplier to impose flux continuity (see also [5] for the extension to the case of non-Newtonian fluids), as well in [19, 20] for a primal Darcy formulation. Ghost penalty methods have been employed for cut FEM methods valid in the regime of large deformations in [2].

Here, and drawing inspiration from the formulation in [7] and [27, 40, 45], we rewrite the poroelasticity equations using three fields (displacement, fluid pressure and total pressure). Compared to previous works [7, 5, 9, 16, 17, 19, 20, 39], which employ the classical displacement formulation, an advantage of the present approach, inherited from [45], is that the formulation is free of poroelastic locking, meaning that it is robust with respect to the Lamé parameters of the poroelastic structure. This is of particular importance when we test variations of the flow response to changes in the material properties of the skeleton and when the solid approaches the incompressibility limit. The present work also stands as an extension of the formulation recently employed in [50] (where only the case of intrinsic incompressible constituent in the poroelastic region were considered) to obtain approximate solutions for heterogeneous poroelasticity coupled with Stokes flow in channels (and using also heterogeneous elastic moduli); while the PDE analysis, numerical aspects, and applicability of the formalism to more realistic scenarios have not yet been addressed. In this work, under adequate assumptions, the analysis of the weak formulation is carried out, using a (time continuous) semi-discrete Galerkin approximation and a weak compactness argument. The well-posedness of the semi-discrete formulation is established using the theory of differential algebraic equations (see, e.g., [15]) and using similar results to those obtained in [7, 53]. A conforming mixed finite element scheme of general order is used. Furthermore, a fully discrete scheme based on backward Euler's time discretisation is considered, and the unique solvability and convergence for the fully discrete scheme are established.

We have organised the contents of this paper in the following manner. Section 2 outlines the model problem, motivating each term in the balance equations and stating the interfacial and boundary conditions. Section 3 states the weak form of the governing equations in Cartesian and axisymmetric coordinates. Then, in Section 4, we address the construction of the finite element scheme, the well-posedness of the continuous and discrete problems, the stability of the fully discrete system in matrix form. Section 5 states the fully-discrete scheme and presents the error estimates. In Section 6 we collect computational results consisting in verification of spatio-temporal convergence and analysis of different cases on simplified and more physiologically accurate geometries, including also a typical application in reservoir modelling. One of the examples involves large displacements near the interface, in which case a harmonic extension operator is used to deform the fluid domain. We close with a summary, some remarks and a discussion on model generalisations in Section 7.

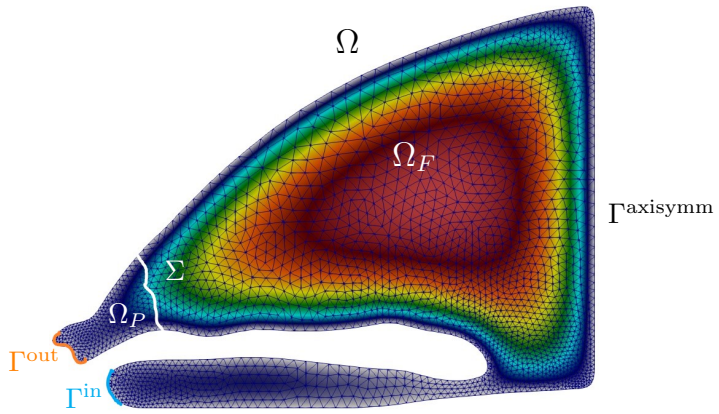

Figure 2.1: Schematic diagram of multidomain configuration on a segmented and meshed geometry, including the location of boundaries and interface. The inlet region Γ^{in} and the symmetry axis Γ^{axisymm} are part of the boundary $\Gamma_F^{\boldsymbol{u}}$, whereas the outlet region Γ^{out} is part of the boundary $\Gamma_P^{\boldsymbol{d}}$.

2. Governing equations

Let us consider a spatial domain $\Omega \subset \mathbb{R}^d$, $d = 2, 3$ disjointly split into Ω_F and Ω_P representing, respectively, the regions where a chamber filled with incompressible fluid and the deformable porous structure are located. We will denote by $\boldsymbol{n}$ the unit normal vector on the boundary $\partial\Omega$, and by $\Sigma = \Omega_F \cap \Omega_P$ the interface between the two subdomains. We also define the boundaries $\Gamma_F = \partial\Omega_F \setminus \Sigma$ and $\Gamma_P = \partial\Omega_P \setminus \Sigma$, and adopt the convention that on Σ the normal vector points from Ω_F to Ω_P. See a rough sketch in Figure 2.1, that represents the geometry of the anterior segment in the eye distinguishing between the anterior chamber Ω_F and the trabecular meshwork Ω_P. The domain is sketched as an axisymmetric region, for which more specific properties will be listed later on.

In presenting the set of governing equations for the coupled fluid - poroelastic system we first focus on the fluid domain, then on the poroelastic domain and, finally, on the initial, boundary and interfacial conditions.

2.1. Fluid domain

In the fluid domain Ω_F, the problem is governed by the momentum and mass conservation equations. Defining the fluid velocity $\boldsymbol{u}$ and the fluid pressure p_F, the resulting system is written as

$$\rho_f(\partial_t \boldsymbol{u} + \boldsymbol{u} \cdot \nabla \boldsymbol{u}) - \mathbf{div}[2\mu_f \boldsymbol{\epsilon}(\boldsymbol{u}) - p_F \mathbf{I}] = \rho_f \boldsymbol{g} \qquad \text{in } \Omega_F \times (0, T], \tag{2.1a}$$

$$\operatorname{div} \boldsymbol{u} = 0 \qquad \text{in } \Omega_F \times (0, T], \tag{2.1b}$$

where ρ_f, μ_f are the density and dynamic viscosity of the fluid (e.g. the aqueous humour if we think to the application for the filtration in the eye and thus Ω_F is the anterior chamber), $\boldsymbol{g}$ is the gravity acceleration, $\boldsymbol{\epsilon}(\boldsymbol{u}) = \frac{1}{2}(\nabla \boldsymbol{u} + \nabla \boldsymbol{u}^{\mathtt{t}})$ is the strain rate tensor and ∂_t indicates derivatives with respect to time. Note that, in typical flow conditions of the eye anterior chamber, the Reynolds number is low (approximately 1.25, while the reduced Reynolds number is between 0.06-0.08. See, e.g., [18, 29, 35, 42]). Therefore, for the stability analysis and for some of the numerical tests later on, we will restrict the fluid model to Stokes' equations.

2.2. Poroelastic domain

The poroelastic domain Ω_P is a biphasic material constituted by a linear elastic solid phase (potentially intrinsically compressible) and an intrinsically incompressible fluid phase. In the context of the eye poromechanics, the trabecular meshwork region occupying Ω_P is constituted by three distinctive tissues, the uveal meshwork, the juxtacanalicular meshwork, and the corneoscleral network; they have different micromechanical properties that, from our modelling perspective, can be regarded as a single poroelastic domain with heterogeneous porosity distribution that, in turn, means possible heterogeneity in the material properties. In addition, we anticipate that, although the fluid viscosity is relevant at the scale of the pore, we assume that the fluid can be treated as inviscid at the macroscale. Calling p_P the fluid pressure and $\boldsymbol{d}$ the solid displacement, here we introduce the formulation that assumes pressure and displacement as primary variables as presented, for example, in [24]

$$\partial_t \left(C_0 p_P + \alpha \operatorname{div} \boldsymbol{d}\right) - \operatorname{div}\left(\frac{\kappa}{\mu_f}(\nabla p_P - \rho_f \boldsymbol{g})\right) = 0 \qquad \text{in } \Omega_P \times (0,T], \tag{2.2a}$$

$$-\mathbf{div}[2\mu_s \boldsymbol{\epsilon}(\boldsymbol{d}) + \lambda \left(\operatorname{div} \boldsymbol{d}\right) \mathbf{I} - \alpha p_P \mathbf{I}] = \rho_m \boldsymbol{f} \qquad \text{in } \Omega_P \times (0,T]. \tag{2.2b}$$

The first equation can be derived from the conservation of mass for the fluid phase once employing the Darcy's law and the relation between fluid content - pressure - hydrostatic deformation of the solid phase. The storage capacity C_0 is related to the intrinsic compressibility of the solid phase, while κ is the permeability (assumed isotropic but heterogeneous). The second equation is the conservation of the momentum for the mixture, where $\boldsymbol{f}$ is a (possibly fluid pressure-dependent) body load, $\boldsymbol{\epsilon}(\boldsymbol{d}) = \frac{1}{2}(\nabla \boldsymbol{d} + \nabla \boldsymbol{d}^{\mathtt{t}})$ is the infinitesimal strain tensor, ρ_s is the density of the porous matrix and ρ_m is the average density of the poroelastic body, λ, μ_s are the Lamé constants of the solid; the term in the divergence in the left-hand side of (2.2b) is known as the effective stress or Terzaghi stress and the parameter α, also known as Biot-Willis poroelastic coefficient, depends on the intrinsic compressibility of the solid phase ($\alpha = 1$ when the solid phase is intrinsically incompressible). We refer an interested reader to [24] or [23] for further details.

For sake of robustness of the formulation with respect to λ, we introduce the *total pressure* $\varphi := \alpha p_P - \lambda \operatorname{div} \boldsymbol{d}$, as an additional unknown in the system (following [40, 45]), and rewrite the pressure-displacement formulation in (2.2) in term of the solid displacement $\boldsymbol{d}$, the fluid pressure p_P, and the total pressure φ, as

$$-\mathbf{div}[2\mu_s \boldsymbol{\epsilon}(\boldsymbol{d}) - \varphi \mathbf{I}] = \rho_m \boldsymbol{f} \qquad \text{in } \Omega_P \times (0,T], \tag{2.3a}$$

$$\varphi - \alpha p_P + \lambda \operatorname{div} \boldsymbol{d} = 0 \qquad \text{in } \Omega_P \times (0,T], \tag{2.3b}$$

$$\left(C_0 + \frac{\alpha^2}{\lambda}\right)\partial_t p_P - \frac{\alpha}{\lambda}\partial_t \varphi - \operatorname{div}\left(\frac{\kappa}{\mu_f}(\nabla p_P - \rho_f \boldsymbol{g})\right) = 0 \qquad \text{in } \Omega_P \times (0,T]. \tag{2.3c}$$

In contrast with the formulations in [16, 7], here we do not employ the fluid velocity in the porous domain as a separate unknown. Consistently with [41], in the framework of linear poroelasticity, the permeability depends on the pressure and the displacement fields only at higher orders; however, it can be heterogeneous, with a spatial distribution dependent, for example, on an initial porosity distribution. We thus simply write

$$\kappa = \kappa(\boldsymbol{x}). \tag{2.4}$$

Likewise, it is also possible to assume heterogeneity of the Lamé constants, as in [50]. In such a case, we need to assume that there exist constants $\lambda_{\min}$ and $\lambda_{\max}$ such that $0 < \lambda_{\min} \leq \lambda \leq \lambda_{\max}$. In the analysis we show that the estimates are independent of $\lambda_{\max}$, i.e., the results are uniform in the almost incompressible limit, even for the heterogeneous case. Heterogeneous permeability and/or heterogeneous Lamé parameters will be used in some of the numerical examples of Section 6.

2.3. Initial, boundary and transmission conditions

To close the system composed by (2.1a), (2.1b), (2.2b), (2.2a), we need to provide suitable initial data, boundary conditions, and adequate transmission assumptions. Without losing generality, we suppose that

$$\boldsymbol{u}(0) = \boldsymbol{u}_0, \quad p_P(0) = p_{P,0} \quad \text{in } \Omega \times \{0\}, \tag{2.5}$$

while for the rest of the variables we will construct compatible initial data. In particular, and for sake of the energy estimates to be addressed in Section 4.2, we will require initial displacement and an initial total pressure (which in turn is computed from the initial displacement and the initial fluid pressure).

On the boundary Γ_F of the fluid domain we can apply conditions on either the velocity, or the stress tensor; we thus decomposed it between $\Gamma_F^{\boldsymbol{u}}$ and $\Gamma_F^{\boldsymbol{\sigma}}$, with $|\Gamma_F^{\boldsymbol{u}}| > 0$, where we impose, respectively, no slip velocities and zero normal total stresses as

$$\boldsymbol{u} = \boldsymbol{0} \qquad \text{on } \Gamma_F^{\boldsymbol{u}} \times (0,T], \tag{2.6a}$$

$$[2\mu_f \boldsymbol{\epsilon}(\boldsymbol{u}) - p_F \mathbf{I}]\boldsymbol{n} = \boldsymbol{0} \qquad \text{on } \Gamma_F^{\boldsymbol{\sigma}} \times (0,T]. \tag{2.6b}$$

Similarly, on the boundary Γ_P of the poroelastic domain we can prescribe conditions on either the displacement or the traction and either the pressure or the fluid flux $\mathbf{q} = -\frac{\kappa}{\mu_f}(\nabla p_P - \rho_f \boldsymbol{g})$. We thus divide the boundary into $\Gamma_P^{p_P}$ and $\Gamma_P^{\boldsymbol{d}}$, with $|\Gamma_P^{p_P}| > 0$ and $|\Gamma_P^{\boldsymbol{d}}| > 0$, where we apply, respectively,

$$\boldsymbol{d} = \boldsymbol{0} \quad \text{and} \quad \frac{\kappa}{\mu_f}(\nabla p_P - \rho_f \boldsymbol{g}) \cdot \boldsymbol{n} = 0 \qquad \text{on } \Gamma_P^{\boldsymbol{d}} \times (0,T], \tag{2.7a}$$

$$[2\mu_s \boldsymbol{\epsilon}(\boldsymbol{d}) - \varphi \mathbf{I}]\boldsymbol{n} = \boldsymbol{0} \quad \text{and} \quad p_P = 0 \qquad \text{on } \Gamma_P^{p_P} \times (0,T]. \tag{2.7b}$$

Next, and following [9, 16, 44, 49], we consider transmission conditions on Σ accounting for the continuity of normal fluxes, momentum conservation, balance of fluid normal stresses, and the so-called Beavers-Joseph-Saffman (BJS) condition for tangential fluid forces

$$\boldsymbol{u} \cdot \boldsymbol{n} = \left(\partial_t \boldsymbol{d} - \frac{\kappa}{\mu_f}(\nabla p_P - \rho_f \boldsymbol{g})\right) \cdot \boldsymbol{n} \qquad \text{on } \Sigma \times (0,T], \tag{2.8a}$$

$$(2\mu_f \boldsymbol{\epsilon}(\boldsymbol{u}) - p_F \mathbf{I})\boldsymbol{n} = (2\mu_s \boldsymbol{\epsilon}(\boldsymbol{d}) - \varphi \mathbf{I})\boldsymbol{n} \qquad \text{on } \Sigma \times (0,T], \tag{2.8b}$$

$$-\boldsymbol{n} \cdot (2\mu_f \boldsymbol{\epsilon}(\boldsymbol{u}) - p_F \mathbf{I})\boldsymbol{n} = p_P \qquad \text{on } \Sigma \times (0,T], \tag{2.8c}$$

$$-\boldsymbol{t}^j \cdot (2\mu_f \boldsymbol{\epsilon}(\boldsymbol{u}) - p_F \mathbf{I})\boldsymbol{n} = \frac{\gamma \mu_f}{\sqrt{\kappa}}(\boldsymbol{u} - \partial_t \boldsymbol{d}) \cdot \boldsymbol{t}^j, \quad 1 \le j \le d-1 \qquad \text{on } \Sigma \times (0,T], \tag{2.8d}$$

where $\gamma > 0$ is the slip rate coefficient (or tangential resistance parameter), and we recall that the normal $\boldsymbol{n}$ on the interface is understood as pointing from the fluid domain Ω_F towards the porous structure Ω_P, while $\boldsymbol{t}^1$ stands for the tangent vector on Σ (for the case of $d = 2$, while for 3D $\boldsymbol{t}^1, \boldsymbol{t}^2$ represent the two tangent vectors on the interface, normal to $\boldsymbol{n}$).

3. Weak formulation

Apart from the nomenclature introduced at the beginning of the section, conventional notation will be adopted throughout the paper. For Lipschitz domains Ξ in $\mathbb{R}^d$, and for $s \in \mathbb{N}$, $k \in \mathbb{N} \cup \infty$ we denote by $W^{k,s}(\Xi)$ the space of all $L^s(\Xi)$ integrable functions with weak derivatives up to order s being also $L^s(\Xi)$ integrable. As usual, for the special case of $s = 2$ we write $H^s(\Xi) := W^{k,2}(\Xi)$ and use boldfaces to refer to vector-valued functions and function spaces, e.g., $\mathbf{H}^s(\Xi) := [H^s(\Xi)]^d$. We will further utilise

the Bochner space-time norms, for a separable Banach space V and $f : (0,T) \to \mathrm{V}$, $\|f\|^2_{L^2(0,T;\mathrm{V})} := \int_0^T \|f(t)\|^2_{\mathrm{V}}\,\mathrm{d}t$ and $\|f\|_{L^\infty(0,T;\mathrm{V})} := \operatorname*{ess\,sup}_{t\in(0,T)} \|f(t)\|_{\mathrm{V}}$. By C we will denote generic constants that are independent of the mesh size.

3.1. Cartesian case

The initial step in deriving the finite element scheme consists in stating a weak form for (2.1a)-(2.3c). We proceed to test these equations against suitable smooth functions and to integrate over the corresponding subdomain. After applying integration by parts wherever adequate, we formally end up with the following remainder on the interface

$$I_\Sigma = -\langle (2\mu_f \boldsymbol{\epsilon}(\boldsymbol{u}) - p_F \mathbf{I})\boldsymbol{n}, \boldsymbol{v}\rangle_\Sigma + \langle (2\mu_s \boldsymbol{\epsilon}(\boldsymbol{d}) - \varphi \mathbf{I})\boldsymbol{n}, \boldsymbol{w}\rangle_\Sigma + \langle \frac{\kappa}{\mu_f}\nabla p_P \cdot \boldsymbol{n}, q_P\rangle_\Sigma,$$

where $\langle\cdot,\cdot\rangle_\Sigma$ denotes the duality pairing between the trace functional space space $H^{1/2}(\Sigma)$ and its dual $H^{-1/2}(\Sigma)$. Then, as in, e.g., [36], we proceed to use each of the transmission conditions (2.8a)-(2.8d), yielding the expression

$$I_\Sigma = \langle p_P, (\boldsymbol{v}-\boldsymbol{w})\cdot\boldsymbol{n}\rangle_\Sigma + \sum_{j=1}^{d-1} \langle \frac{\gamma\mu_f}{\sqrt{\kappa}}(\boldsymbol{u}-\partial_t\boldsymbol{d})\cdot\boldsymbol{t}^j, (\boldsymbol{v}-\boldsymbol{w})\cdot\boldsymbol{t}^j\rangle_\Sigma - \langle (\boldsymbol{u}-\partial_t\boldsymbol{d})\cdot\boldsymbol{n}, q_P\rangle_\Sigma.$$

This interfacial term is well-defined because of the regularity of the entities involved, and this implies that we do not require additional Lagrange multipliers to realise the coupling conditions. Also, in view of the boundary conditions we define the Hilbert spaces

$$\mathbf{H}^1_\star(\Omega_F) = \{\boldsymbol{v}\in\mathbf{H}^1(\Omega_F) : \boldsymbol{v}|_{\Gamma_F^{\boldsymbol{u}}} = \mathbf{0}\}, \quad \mathbf{H}^1_\star(\Omega_P) = \{\boldsymbol{w}\in\mathbf{H}^1(\Omega_P) : \boldsymbol{w}|_{\Gamma_P^{\boldsymbol{d}}} = \mathbf{0}\},$$
$$H^1_\star(\Omega_P) = \{q_P \in H^1(\Omega_P) : q_P|_{\Gamma_P^{pP}} = 0\},$$

associated with the classical norms in $\mathbf{H}^1(\Omega_F), \mathbf{H}^1(\Omega_P)$, and $H^1(\Omega_P)$, respectively. Consequently we have the following mixed weak form: For $t\in[0,T]$, find $\boldsymbol{u}\in\mathbf{H}^1_\star(\Omega_F)$, $p_F\in L^2(\Omega_F)$, $\boldsymbol{d}\in\mathbf{H}^1_\star(\Omega_P)$, $p_P\in H^1_\star(\Omega_P)$, $\varphi\in L^2(\Omega_P)$, such that

$$\begin{aligned}
&a_1^F(\partial_t\boldsymbol{u},\boldsymbol{v}) + a_2^F(\boldsymbol{u},\boldsymbol{v}) + c^F(\boldsymbol{u},\boldsymbol{u};\boldsymbol{v}) + b_1^F(\boldsymbol{v},p_F)\\
&\qquad + b_2^\Sigma(\boldsymbol{v},p_P) + b_3^\Sigma(\boldsymbol{v},\partial_t\boldsymbol{d}) = F^F(\boldsymbol{v}) && \forall\boldsymbol{v}\in\mathbf{H}^1_\star(\Omega_F), && (3.1a)\\
&-b_1^F(\boldsymbol{u},q_F) = 0 && \forall q_F\in L^2(\Omega_F), && (3.1b)\\
&b_3^\Sigma(\boldsymbol{u},\boldsymbol{w}) + b_4^\Sigma(\boldsymbol{w},p_P) + a_1^P(\boldsymbol{d},\boldsymbol{w})\\
&\qquad + a_2^\Sigma(\partial_t\boldsymbol{d},\boldsymbol{w}) + b_1^P(\boldsymbol{w},\varphi) = F^P(\boldsymbol{w}) && \forall\boldsymbol{w}\in\mathbf{H}^1_\star(\Omega_P), && (3.1c)\\
&-b_2^\Sigma(\boldsymbol{u},q_P) - b_4^\Sigma(\partial_t\boldsymbol{d},q_P) + a_3^P(\partial_t p_P,q_P)\\
&\qquad + a_4^P(p_P,q_P) - b_2^P(\partial_t\varphi,q_P) = G(q_P) && \forall q_P\in H^1_\star(\Omega_P), && (3.1d)\\
&-b_1^P(\boldsymbol{d},\psi) - b_2^P(\psi,p_P) + a_5^P(\varphi,\psi) = 0 && \forall\psi\in L^2(\Omega_P), && (3.1e)
\end{aligned}$$

where the bilinear and trilinear forms and linear functionals are defined as

$$a_1^F(\boldsymbol{u},\boldsymbol{v}) = \rho_f\int_{\Omega_F}\boldsymbol{u}\cdot\boldsymbol{v}, \quad a_2^F(\boldsymbol{u},\boldsymbol{v}) = 2\mu_f\int_{\Omega_F}\boldsymbol{\epsilon}(\boldsymbol{u}):\boldsymbol{\epsilon}(\boldsymbol{v}) + \sum_{j=1}^{d-1}\langle\frac{\gamma\mu_f}{\sqrt{\kappa}}\boldsymbol{u}\cdot\boldsymbol{t}^j,\boldsymbol{v}\cdot\boldsymbol{t}^j\rangle_\Sigma,$$

$$c^F(\boldsymbol{u},\boldsymbol{w};\boldsymbol{v})=\rho_f\int_{\Omega_F}(\boldsymbol{u}\cdot\nabla\boldsymbol{w})\cdot\boldsymbol{v},\quad b_1^F(\boldsymbol{v},q_F)=-\int_{\Omega_F}q_F\,\mathrm{div}\,\boldsymbol{v},\quad b_1^P(\boldsymbol{w},\psi)=-\int_{\Omega_P}\psi\,\mathrm{div}\,\boldsymbol{w},$$

$$b_2^\Sigma(\boldsymbol{v},q_P)=\langle q_P,\boldsymbol{v}\cdot\boldsymbol{n}\rangle_\Sigma,\quad b_3^\Sigma(\boldsymbol{v},\boldsymbol{w})=-\sum_{j=1}^{d-1}\langle\frac{\gamma\mu_f}{\sqrt{\kappa}}\boldsymbol{v}\cdot\boldsymbol{t}^j,\boldsymbol{w}\cdot\boldsymbol{t}^j\rangle_\Sigma,\quad b_4^\Sigma(\boldsymbol{w},q_P)=-\langle q_P,\boldsymbol{w}\cdot\boldsymbol{n}\rangle_\Sigma,$$

$$a_1^P(\boldsymbol{d},\boldsymbol{w})=2\mu_s\int_{\Omega_P}\boldsymbol{\epsilon}(\boldsymbol{d}):\boldsymbol{\epsilon}(\boldsymbol{w}),\quad a_2^\Sigma(\boldsymbol{d},\boldsymbol{w})=\sum_{j=1}^{d-1}\langle\frac{\gamma\mu_f}{\sqrt{\kappa}}\boldsymbol{d}\cdot\boldsymbol{t}^j,\boldsymbol{w}\cdot\boldsymbol{t}^j\rangle_\Sigma, \tag{3.2}$$

$$a_3^P(p_P,q_P)=\big(C_0+\frac{\alpha^2}{\lambda}\big)\int_{\Omega_P}p_Pq_P,\quad a_4^P(p_P,q_P)=\int_{\Omega_P}\frac{\kappa}{\mu_f}\nabla p_P\cdot\nabla q_P,$$

$$b_2^P(\psi,q_P)=\frac{\alpha}{\lambda}\int_{\Omega_P}\psi q_P,\quad a_5^P(\varphi,\psi)=\frac{1}{\lambda}\int_{\Omega_P}\varphi\psi,\quad F^F(\boldsymbol{v})=\rho_f\int_{\Omega_F}\boldsymbol{g}\cdot\boldsymbol{v},$$

$$F^P(\boldsymbol{w})=\rho_s\int_{\Omega_P}\boldsymbol{f}\cdot\boldsymbol{w},\quad G(q_P)=\int_{\Omega_P}\rho_f\frac{\kappa}{\mu_f}\boldsymbol{g}\cdot\nabla q_P-\langle\rho_f\frac{\kappa}{\mu_f}\boldsymbol{g}\cdot\boldsymbol{n},q_P\rangle_\Sigma.$$

3.2. Axisymmetric case

For the specific application of interfacial flow in the eye, the radial symmetry of the domain and of the flow conditions could be better represented using axisymmetric formulations as in [8, 25, 42]. Then, the domain as well as the expected flow properties are all symmetric with respect to the axis of symmetry $\Gamma^{\mathrm{axisymm}}$. The model equations can be written in the meridional domain Ω (making abuse of notation, and referring to Figure 2.1). In such a setting the fluid velocity and solid displacement only possess radial and vertical components and we recall that the divergence operator of the generic vector field $\boldsymbol{v}$ in axisymmetric coordinates (in radial and height variables r,z) is

$$\mathrm{div_a}\,\boldsymbol{v}:=\partial_z v_z+\frac{1}{r}\partial_r(rv_r),$$

while the notation of the gradient coincides with that in Cartesian coordinates. The weak formulation (3.1) adopts the following modifications (again making abuse of notation, the unknowns are denoted the same as in the Cartesian case): Find $\boldsymbol{u}\in\widehat{\mathbf{V}}$, $p_F\in\widehat{\mathrm{Q}}^F$, $\boldsymbol{d}\in\widehat{\mathbf{W}}$, $p_P\in\widehat{\mathrm{Q}}^P$, $\varphi\in\widehat{\mathrm{Z}}$, such that

$$\rho_f\int_{\Omega_F}\partial_t\boldsymbol{u}\cdot\boldsymbol{v}\,r\,\mathrm{d}r\,\mathrm{d}z+2\mu_f\int_{\Omega_F}\boldsymbol{\epsilon}(\boldsymbol{u}):\boldsymbol{\epsilon}(\boldsymbol{v})r\,\mathrm{d}r\,\mathrm{d}z+2\mu_f\int_{\Omega_F}\frac{1}{r}u_rv_r\,\mathrm{d}r\,\mathrm{d}z-\int_{\Omega_F}p_F\,\mathrm{div_a}\,\boldsymbol{v}\,r\,\mathrm{d}r\,\mathrm{d}z$$
$$+\int_\Sigma\frac{\gamma\mu_f}{\sqrt{\kappa}}(\boldsymbol{u}-\partial_t\boldsymbol{d})\cdot\boldsymbol{t}\boldsymbol{v}\cdot\boldsymbol{t}r\,\mathrm{d}r\,\mathrm{d}z+\int_\Sigma p_F\boldsymbol{v}\cdot\boldsymbol{n}r\,\mathrm{d}r\,\mathrm{d}z=\rho_f\int_{\Omega_F}\boldsymbol{g}\cdot\boldsymbol{v}r\,\mathrm{d}r\,\mathrm{d}z\quad\forall\boldsymbol{v}\in\widehat{\mathbf{V}}, \tag{3.3a}$$

$$-\int_{\Omega_F}q_F\,\mathrm{div_a}\,\boldsymbol{u}\,r\,\mathrm{d}r\,\mathrm{d}z=0\qquad\forall q_F\in\widehat{\mathrm{Q}}^F, \tag{3.3b}$$

$$2\mu_s\int_{\Omega_P}\boldsymbol{\epsilon}(\boldsymbol{d}):\boldsymbol{\epsilon}(\boldsymbol{w})\,r\,\mathrm{d}r\,\mathrm{d}z+2\mu_s\int_{\Omega_P}\frac{1}{r}d_rw_r\,\mathrm{d}r\,\mathrm{d}z-\int_\Sigma\frac{\gamma\mu_f}{\sqrt{\kappa}}(\boldsymbol{u}-\partial_t\boldsymbol{d})\cdot\boldsymbol{t}\boldsymbol{w}\cdot\boldsymbol{t}r\,\mathrm{d}r\,\mathrm{d}z$$
$$-\int_{\Omega_P}\varphi\,\mathrm{div_a}\,\boldsymbol{w}\,r\,\mathrm{d}r\,\mathrm{d}z-\int_\Sigma p_P\boldsymbol{w}\cdot\boldsymbol{n}\,\mathrm{d}r\,\mathrm{d}z=\rho_s\int_{\Omega_P}\boldsymbol{f}\cdot\boldsymbol{w}\,r\,\mathrm{d}r\,\mathrm{d}z\qquad\forall\boldsymbol{w}\in\widehat{\mathbf{W}}, \tag{3.3c}$$

$$\big(C_0+\frac{\alpha^2}{\lambda}\big)\int_{\Omega_P}\partial_tp_Pq_P\,r\,\mathrm{d}r\,\mathrm{d}z+\int_{\Omega_P}\frac{\kappa}{\mu_f}\nabla p_P\cdot\nabla q_P\,r\,\mathrm{d}r\,\mathrm{d}z-\frac{\alpha}{\lambda}\int_{\Omega_P}\partial_t\varphi q_P\,r\,\mathrm{d}r\,\mathrm{d}z$$
$$+\int_\Sigma q_P(\boldsymbol{u}-\partial_t\boldsymbol{d})\cdot\boldsymbol{n}r\,\mathrm{d}r\,\mathrm{d}z=\int_{\Omega_P}\rho_f\boldsymbol{g}\cdot\nabla q_Pr\,\mathrm{d}r\,\mathrm{d}z-\int_\Sigma\rho_f\boldsymbol{g}\cdot\boldsymbol{n}q_Pr\,\mathrm{d}r\,\mathrm{d}z\quad\forall q_P\in\widehat{\mathrm{Q}}^P, \tag{3.3d}$$

$$-\int_{\Omega_F}\psi\,\mathrm{div_a}\,\boldsymbol{v}\,r\,\mathrm{d}r\,\mathrm{d}z+\frac{\alpha}{\lambda}\int_{\Omega_P}p_P\psi\,r\,\mathrm{d}r\,\mathrm{d}z-\frac{1}{\lambda}\int_{\Omega_P}\varphi\psi\,r\,\mathrm{d}r\,\mathrm{d}z=0\qquad\forall\psi\in\widehat{\mathrm{Z}}.\tag{3.3e}$$

Here the functional spaces are now defined as

$$\widehat{\mathbf{V}}:=\{\boldsymbol{v}\in V_1^1(\Omega_F)\times\mathrm{H}_1^1(\Omega_F):\boldsymbol{v}|_{\Gamma_F^{\boldsymbol{u}}}=\mathbf{0}\text{ and }\boldsymbol{v}\cdot\boldsymbol{n}|_{\Gamma^{\mathrm{axisymm}}}=0\},\quad\widehat{\mathrm{Q}}^F:=L_1^2(\Omega_F),$$
$$\widehat{\mathbf{W}}:=\{\boldsymbol{w}\in V_1^1(\Omega_P)\times\mathrm{H}_1^1(\Omega_P):\boldsymbol{w}|_{\Gamma_F^{\boldsymbol{d}}}=\mathbf{0}\},\ \widehat{\mathrm{Q}}^P:=\{q_P\in\mathrm{H}_1^1(\Omega_P):q_P|_{\Gamma_P^{pP}}=0\},\ \widehat{\mathrm{Z}}:=L_1^2(\Omega_P),$$

where, for $m\in\mathbb{R}$, $1\le p<\infty$ the weighted functional spaces adopt the specification

$$L_m^p(\Omega_i)=\{v:\|v\|_{m,p,\Omega_i}^p:=\int_{\Omega_i}|v|^p r^m\,\mathrm{d}r\,\mathrm{d}z<\infty\},$$

and

$$\mathrm{H}_1^1(\Omega_i):=\{v\in L_1^2(\Omega_i):\nabla v\in\mathbf{L}_1^2(\Omega_i)\},\quad V_1^1(\Omega_i):=\mathrm{H}_1^1(\Omega_i)\cap L_{-1}^2(\Omega_i).$$

4. Well-posedness of the weak formulation

The following analysis is confined to the Cartesian case. Furthermore, we focus on the quasi-static Biot-Stokes model, i.e., we neglect the terms a_1^F and c^F in (3.1a), as this is the typical flow regime for the application of interest. We also restrict our attention to the case $\tilde{\alpha}=1$. The solvability analysis is based on a Galerkin argument, where one considers the semi-discrete continuous in time formulation with a discretisation parameter h. We establish that it has a unique solution and derive stability bounds. Then, owing to a weak compactness argument, we pass to the limit $h\to 0$ and obtain existence and uniqueness of a weak solution.

4.1. Semi-discrete mixed finite element formulation

In addition to the assumptions stated before on the domain geometry, to avoid additional technicalities, we operate under the condition that Ω is a polytope. We denote by $\{\mathcal{T}_h\}_{h>0}$ a shape-regular family of finite element partitions of $\bar{\Omega}$, conformed by tetrahedra (or triangles in 2D) K of diameter h_K, with mesh size $h:=\max\{h_K:K\in\mathcal{T}_h\}$. The finite-dimensional subspaces for fluid velocity, fluid pressure, porous displacement, porous fluid pressure, and total pressure are denoted $\mathbf{V}_h,\mathrm{Q}_h^F,\mathbf{W}_h,\mathrm{Q}_h^P,\mathrm{Z}_h$, respectively. It is sufficient for the following analysis that the pairs $(\mathbf{V}_h,\mathrm{Q}_h^F)$ and $(\mathbf{W}_h,\mathrm{Z}_h)$ are Stokes inf-sup stable, in the sense that there exist positive constants β_F and β_P independent of h such that

$$\forall\,q_{F,h}\in\mathrm{Q}_h^F,\quad\sup_{\mathbf{0}\neq\boldsymbol{v}_h\in\mathbf{V}_h}\frac{b_1^F(\boldsymbol{v}_h,q_{F,h})}{\|\boldsymbol{v}_h\|_{\mathbf{H}^1(\Omega_F)}}\ge\beta_F\|q_{F,h}\|_{L^2(\Omega_F)},\tag{4.1a}$$

$$\forall\,\psi_h\in\mathrm{Z}_h,\quad\sup_{\mathbf{0}\neq\boldsymbol{w}_h\in\mathbf{W}_h}\frac{b_1^P(\boldsymbol{w}_h,\psi_h)}{\|\boldsymbol{w}_h\|_{\mathbf{H}^1(\Omega_P)}}\ge\beta_P\|\psi_h\|_{L^2(\Omega_P)}.\tag{4.1b}$$

Feasible choices are Taylor-Hood, the MINI element, Crouzeix-Raviart, Scott-Vogelius, Guzmán-Neilan, Bernardi-Raugel, equal-order stabilised methods (including total pressure projection stabilisation), divergence-conforming stabilised methods, and many others. If taking, for example, generalised Taylor-Hood elements of degree $(k,k-1)$ for $\mathbf{V}_h\times\mathrm{Q}_h^F$ and $\mathbf{W}_h\times\mathrm{Z}_h$, alongside a piecewise continuous and polynomial space of degree k for Q_h^P, then their interpolation properties will yield a method of overall order k in space when the displacement and velocity errors are measured in the $\mathbf{H}^1$-norm, the total pressure and Stokes fluid pressure in the L^2-norm, and the Biot fluid pressure in the H^1-norm. A more

general case, with different polynomial degrees for the different finite element spaces, is addressed in Section 5.1, below.

We look for $(\boldsymbol{u}_h, p_{F,h}, \boldsymbol{d}_h, p_{P,h}, \varphi_h) : [0,T] \to \mathbf{V}_h \times \mathrm{Q}_h^F \times \mathbf{W}_h \times \mathrm{Q}_h^P \times \mathrm{Z}_h =: \mathbf{H}_h$ such that for a.e. $t \in (0,T]$,

$$a_2^F(\boldsymbol{u}_h, \boldsymbol{v}_h) + b_1^F(\boldsymbol{v}_h, p_{F,h}) + b_2^\Sigma(\boldsymbol{v}_h, p_{P,h}) + b_3^\Sigma(\boldsymbol{v}_h, \partial_t \boldsymbol{d}_h) = F^F(\boldsymbol{v}_h) \qquad \forall \boldsymbol{v}_h \in \mathbf{V}_h, \tag{4.2a}$$

$$-b_1^F(\boldsymbol{u}_h, q_{F,h}) = 0 \qquad \forall q_{F,h} \in \mathrm{Q}_h^F, \tag{4.2b}$$

$$b_3^\Sigma(\boldsymbol{u}_h, \boldsymbol{w}_h) + b_4^\Sigma(\boldsymbol{w}_h, p_{P,h}) + a_1^P(\boldsymbol{d}_h, \boldsymbol{w}_h) + a_2^\Sigma(\partial_t \boldsymbol{d}_h, \boldsymbol{w}_h) + b_1^P(\boldsymbol{w}_h, \varphi_h) = F^P(\boldsymbol{w}_h) \qquad \forall \boldsymbol{w}_h \in \mathbf{W}_h, \tag{4.2c}$$

$$-b_2^\Sigma(\boldsymbol{u}_h, q_{P,h}) - b_4^\Sigma(\partial_t \boldsymbol{d}_h, q_{P,h}) + a_3^P(\partial_t p_{P,h}, q_{P,h}) + a_4^P(p_{P,h}, q_{P,h}) - b_2^P(\partial_t \varphi_h, q_{P,h}) = G(q_{P,h}) \qquad \forall q_{P,h} \in \mathrm{Q}_h^P, \tag{4.2d}$$

$$-b_1^P(\boldsymbol{d}_h, \psi_h) - b_2^P(\psi_h, p_{P,h}) + a_5^P(\varphi_h, \psi_h) = 0 \qquad \forall \psi_h \in \mathrm{Z}_h. \tag{4.2e}$$

This is a system of differential-algebraic equations (DAE) that can be written in an operator form as

$$\partial_t \mathcal{N} \underline{\boldsymbol{u}}_h(t) + \mathcal{M} \underline{\boldsymbol{u}}_h(t) = \mathcal{F}(t), \tag{4.3}$$

with $\underline{\boldsymbol{u}}_h := [\boldsymbol{u}_h \; p_{F,h} \; \boldsymbol{d}_h \; p_{P,h} \; \varphi_h]^{\mathtt{t}}$,

$$\mathcal{N} = \left[\begin{array}{cc:ccc} \mathbf{0} & \mathbf{0} & (\mathcal{B}_3^\Sigma)' & \mathbf{0} & \mathbf{0} \\ \mathbf{0} & \mathbf{0} & \mathbf{0} & \mathbf{0} & \mathbf{0} \\ \hdashline \mathbf{0} & \mathbf{0} & \mathcal{A}_2^\Sigma & \mathbf{0} & \mathbf{0} \\ \mathbf{0} & \mathbf{0} & -\mathcal{B}_4^\Sigma & \mathcal{A}_3^P & -(\mathcal{B}_2^P)' \\ \mathbf{0} & \mathbf{0} & \mathbf{0} & \mathbf{0} & \mathbf{0} \end{array}\right], \quad \mathcal{M} = \left[\begin{array}{cc:ccc} \mathcal{A}_2^F & (\mathcal{B}_1^F)' & \mathbf{0} & (\mathcal{B}_2^\Sigma)' & \mathbf{0} \\ -\mathcal{B}_1^F & \mathbf{0} & \mathbf{0} & \mathbf{0} & \mathbf{0} \\ \hdashline \mathcal{B}_3^\Sigma & \mathbf{0} & \mathcal{A}_1^P & (\mathcal{B}_4^\Sigma)' & (\mathcal{B}_1^P)' \\ -\mathcal{B}_2^\Sigma & \mathbf{0} & \mathbf{0} & \mathcal{A}_4^P & \mathbf{0} \\ \mathbf{0} & \mathbf{0} & -\mathcal{B}_1^P & -\mathcal{B}_2^P & \mathcal{A}_5^P \end{array}\right], \quad \mathcal{F} = \left[\begin{array}{c} \mathcal{F}^F \\ \mathbf{0} \\ \mathcal{F}^P \\ \mathcal{G} \\ \mathbf{0} \end{array}\right],$$

where the operators in calligraphic letters are induced by the forms in (3.2). The symbol $(\cdot)'$ denotes the dual operator resulting in the transpose block matrix of a given elementary block.

We next discuss the initial condition for (4.3). Recall from (2.5) that we are given initial data $p_{P,0}$ and note that we do not use the initial data $\boldsymbol{u}_0$, since we are considering the quasi-static Stokes model. We assume that $p_{P,0} \in H^1_\star(\Omega_p)$ and take $p_{P,h}(0) = p_{P,h,0}$, where $p_{P,h,0} \in \mathrm{Q}_h^P$ is the L^2-projection of $p_{P,0}$. In addition, we need initial data $\boldsymbol{d}_{h,0} \in \mathbf{W}_h$ and $\varphi_{h,0} \in Z_h$ such that $\boldsymbol{d}_h(0) = \boldsymbol{d}_{h,0}$ and $\varphi_h(0) = \varphi_{h,0}$. The construction of such data will be discussed in Theorem 4.1.

4.2. Well-posedness of the semi-discrete problem

The well-posedness of the semi-discrete formulation could be analysed by recasting the system as a general parabolic operator with degenerate time derivative, as recently proposed in [5] for the interaction of non-Newtonian fluids and poroelastic media. This would require, however, to include the solid velocity as a new unknown. Instead, we study it using the theory of DAE, following the approach from [7].

In the forthcoming analysis we will appeal to the Poincaré inequality

$$\|\nabla q_P\|_{L^2(\Omega_P)} \geq c_P \|q_P\|_{H^1(\Omega_P)}, \quad \forall\, q_P \in H^1_\star(\Omega_P), \tag{4.4}$$

Korn's inequality

$$\|\boldsymbol{\epsilon}(\boldsymbol{v})\|_{\mathbf{L}^2(\Omega_F)} \geq c_K^F \|\boldsymbol{v}\|_{\mathbf{H}^1(\Omega_F)}, \qquad \|\boldsymbol{\epsilon}(\boldsymbol{w})\|_{\mathbf{L}^2(\Omega_P)} \geq c_K^P \|\boldsymbol{w}\|_{\mathbf{H}^1(\Omega_P)}, \tag{4.5}$$

for all $\boldsymbol{v} \in \mathbf{H}^1_\star(\Omega_F)$, $\boldsymbol{w} \in \mathbf{H}^1_\star(\Omega_P)$, and the trace inequality

$$\|\boldsymbol{v}\|_{\mathbf{L}^2(\Sigma)} \leq C_\Sigma^F \|\boldsymbol{v}\|_{\mathbf{H}^1(\Omega_F)}, \qquad \|q_P\|_{L^2(\Sigma)} \leq C_\Sigma^P \|q_P\|_{H^1(\Omega_P)}, \tag{4.6}$$

for all $\boldsymbol{v} \in \mathbf{H}^1(\Omega_F)$, $q_P \in H^1(\Omega_P)$. We also assume that there exist constants $0 < \kappa_1 < \kappa_2 < \infty$ such that

$$\kappa_1 \leq \kappa(\boldsymbol{x}) \leq \kappa_2 \quad \text{for a.e. } \boldsymbol{x} \in \Omega_P. \tag{4.7}$$

Lemma 4.1. *The bilinear forms that appear in (4.2) are continuous in the spaces* $\mathbf{V}$, Q^F, $\mathbf{W}$, Q^P, *and* Z. *If* $\boldsymbol{f} : [0,T] \to \mathbf{L}^2(\Omega_P)$, *then the linear functionals on the right-hand sides are also continuous.*

Proof. The statement of the lemma follows from the use of the Cauchy-Schwarz inequality and the trace inequality (4.6). □

Theorem 4.1. *For each* $\boldsymbol{f} \in H^1(0,T;\mathbf{L}^2(\Omega_P))$ *and* $p_{P,0} \in H^1_\star(\Omega_p)$, *there exist initial data* $\boldsymbol{u}_{h,0} \in \mathbf{V}_h$, $p_{F,h,0} \in \mathrm{Q}_h^F$, $\boldsymbol{d}_{h,0} \in \mathbf{W}_h$, *and* $\varphi_{h,0} \in Z_h$ *such that the semi-discrete problem (4.3) with initial conditions* $p_{P,h}(0) = p_{P,h,0}$, $\boldsymbol{d}_h(0) = \boldsymbol{d}_{h,0}$, *and* $\varphi_h(0) = \varphi_{h,0}$ *has a unique solution satisfying*

$$\begin{aligned}
&\|\boldsymbol{u}_h\|_{L^2(0,T;\mathbf{H}^1(\Omega_F))} + \|p_{F,h}\|_{L^2(0,T;L^2(\Omega_F))} + \|\boldsymbol{d}_h\|_{L^\infty(0,T;\mathbf{H}^1(\Omega_P))} \\
&\quad + \sum_{j=1}^{d-1} \|(\boldsymbol{u}_h - \partial_t \boldsymbol{d}_h)\cdot \boldsymbol{t}^j\|_{L^2(0,T;L^2(\Sigma))} + \|p_{P,h}\|_{L^\infty(0,T;L^2(\Omega_P))} + \|p_{P,h}\|_{L^2(0,T;H^1(\Omega_P))} \\
&\quad + \|\varphi_h\|_{L^2(0,T;L^2(\Omega_P))} + \frac{1}{\sqrt{\lambda}} \|\alpha\, p_{P,h} - \varphi_h\|_{L^\infty(0,T;L^2(\Omega_P))} \\
&\leq C\left(\|\boldsymbol{g}\|_{L^2(0,T;\mathbf{L}^2(\Omega))} + \|\boldsymbol{g}\cdot\boldsymbol{n}\|_{L^2(0,T;L^2(\Sigma))} + \|\boldsymbol{f}\|_{H^1(0,T;\mathbf{L}^2(\Omega_P))} + \|p_{P,0}\|_{H^1(\Omega_P)}\right),
\end{aligned} \tag{4.8a}$$

and

$$\begin{aligned}
&\|\boldsymbol{u}_h\|_{L^\infty(0,T;\mathbf{H}^1(\Omega_F))} + \|p_{F,h}\|_{L^\infty(0,T;L^2(\Omega_F))} + \|\partial_t \boldsymbol{d}_h\|_{L^2(0,T;\mathbf{H}^1(\Omega_P))} \\
&\quad + \sum_{j=1}^{d-1} \|(\boldsymbol{u}_h - \partial_t \boldsymbol{d}_h)\cdot \boldsymbol{t}^j\|_{L^\infty(0,T;L^2(\Sigma))} + \|\partial_t p_{P,h}\|_{L^2(0,T;L^2(\Omega_P))} + \|p_{P,h}\|_{L^\infty(0,T;H^1(\Omega_P))} \\
&\quad + \|\varphi_h\|_{L^\infty(0,T;L^2(\Omega_P))} + \frac{1}{\sqrt{\lambda}} \|\alpha\, \partial_t p_{P,h} - \partial_t \varphi_h\|_{L^2(0,T;L^2(\Omega_P))} \\
&\leq C\left(\|\boldsymbol{g}\|_{L^2(0,T;\mathbf{L}^2(\Omega))} + \|\boldsymbol{g}\cdot\boldsymbol{n}\|_{L^2(0,T;L^2(\Sigma))} + \|\boldsymbol{f}\|_{H^1(0,T;\mathbf{L}^2(\Omega_P))} + \|p_{P,0}\|_{H^1(\Omega_P)}\right),
\end{aligned} \tag{4.8b}$$

with a constant C *independent of* $\lambda_{\max}$ *and* h.

Proof. To establish existence, we employ [15, Th. 2.3.1], which asserts that (4.3) has a solution if the matrix pencil $s\mathcal{N} + \mathcal{M}$ is nonsingular for some $s \neq 0$. The solvability of the associated initial value problem requires initial data that is consistent with the DAE system. To deal with this issue, we first consider a related DAE system by including new variables $\theta_h^j \in \mathbf{W}_h \cdot \boldsymbol{t}^j$, $j = 1, \ldots d-1$ and equations

$$\langle \theta_h^j, \boldsymbol{w}_h \cdot \boldsymbol{t}^j \rangle_\Sigma = \langle \partial_t \boldsymbol{d}_h \cdot \boldsymbol{t}^j, \boldsymbol{w}_h \cdot \boldsymbol{t}^j \rangle_\Sigma \quad \forall \boldsymbol{w}_h \in \mathbf{W}_h, \quad j = 1, \ldots d-1, \tag{4.9}$$

and replacing $\partial_t \boldsymbol{d}_h \cdot \boldsymbol{t}^j$ with θ_h^j in (4.2a) and (4.2c). Let $\underline{\tilde{\boldsymbol{u}}}_h := [\boldsymbol{u}_h\ p_{F,h}\ \boldsymbol{d}_h\ p_{P,h}\ \varphi_h\ \theta_h^1 \cdots \theta_h^{d-1}]^{\mathtt{t}}$ and denote the extended DAE system by

$$\partial_t \tilde{\mathcal{N}} \underline{\tilde{\boldsymbol{u}}}_h(t) + \tilde{\mathcal{M}} \underline{\tilde{\boldsymbol{u}}}_h(t) = \tilde{\mathcal{F}}(t). \tag{4.10}$$

Clearly any solution of (4.10) also solves (4.3). We will apply [15, Th. 2.3.1] to (4.10). We will show that the matrix $\tilde{\mathcal{N}}+\tilde{\mathcal{M}}$ is nonsingular by proving that the system $(\tilde{\mathcal{N}}+\tilde{\mathcal{M}})\underline{\tilde{\boldsymbol{u}}}_h=\mathbf{0}$ has only the zero solution. By eliminating θ_h^j, this system results in $(\mathcal{N}+\mathcal{M})\underline{\boldsymbol{u}}_h=\mathbf{0}$. Using that

$$\mathcal{N}+\mathcal{M}=\left[\begin{array}{cc:ccc} \mathcal{A}_2^F & (\mathcal{B}_1^F)' & (\mathcal{B}_3^\Sigma)' & (\mathcal{B}_2^\Sigma)' & \mathbf{0} \\ -\mathcal{B}_1^F & \mathbf{0} & \mathbf{0} & \mathbf{0} & \mathbf{0} \\ \hdashline \mathcal{B}_3^\Sigma & \mathbf{0} & \mathcal{A}_1^P+\mathcal{A}_2^\Sigma & (\mathcal{B}_4^\Sigma)' & (\mathcal{B}_1^P)' \\ -\mathcal{B}_2^\Sigma & \mathbf{0} & -\mathcal{B}_4^\Sigma & \mathcal{A}_3^P+\mathcal{A}_4^P & -(\mathcal{B}_2^P)' \\ \mathbf{0} & \mathbf{0} & -\mathcal{B}_1^P & -\mathcal{B}_2^P & \mathcal{A}_5^P \end{array}\right],$$

the equation $\underline{\boldsymbol{u}}_h^{\mathtt{t}}(\mathcal{N}+\mathcal{M})\underline{\boldsymbol{u}}_h=0$ gives

$$\begin{aligned} &2\mu_f\int_{\Omega_F}\boldsymbol{\epsilon}(\boldsymbol{u}_h):\boldsymbol{\epsilon}(\boldsymbol{u}_h)+\sum_{j=1}^{d-1}\langle\frac{\gamma\mu_f}{\sqrt{\kappa}}(\boldsymbol{u}_h-\boldsymbol{d}_h)\cdot\boldsymbol{t}^j\,,(\boldsymbol{u}_h-\boldsymbol{d}_h)\cdot\boldsymbol{t}^j\rangle_\Sigma+2\mu_s\int_{\Omega_P}\boldsymbol{\epsilon}(\boldsymbol{d}_h):\boldsymbol{\epsilon}(\boldsymbol{d}_h)\\ &\quad+C_0\int_{\Omega_P}p_{P,h}^2+\int_{\Omega_P}\frac{\kappa}{\mu_f}\nabla p_{P,h}\cdot\nabla p_{P,h}+\frac{1}{\lambda}\int_{\Omega_P}(\alpha\,p_{P,h}-\varphi_h)^2=0,\end{aligned}$$

which implies that $\boldsymbol{u}_h=\mathbf{0}$, $\boldsymbol{d}_h=\mathbf{0}$, $p_{P,h}=0$, and $\varphi_h=0$. Equations (4.9) imply that $\theta_h^j=0$. The inf-sup condition (4.1a) with $q_{F,h}=p_{F,h}$ and (4.2a) give $p_{F,h}=0$. Therefore (4.10) has a solution.

We proceed with the construction of the initial data. We first note that there exists a solution to (4.10) satisfying $p_{P,h}(0)=p_{P,h,0}$, since this initial condition is associated with the differential equation (4.2d). We need to find initial values for the rest of the variables that are consistent with the DAE system. Let us set $\theta_h^j(0)=\theta_{h,0}^j=0$ and consider the Stokes problem (4.2a)–(4.2b) for $\boldsymbol{u}_{h,0}$ and $p_{F,h,0}$ with data $p_{P,h,0}$ and $\theta_{h,0}^j$, which is now decoupled and well-posed from the Stokes finite element theory. Finally, let $\boldsymbol{d}_{h,0}$ and $\varphi_{h,0}$ solve the problem coupling (4.2c) and (4.2e) with data $p_{P,h,0}$, $\theta_{h,0}^j$, and $\boldsymbol{u}_{h,0}$. The well-posedness of this problem follows from the theory of saddle-point problems [12], due to the inf-sup condition (4.1b), see also [45]. We further note that taking $t\to 0$ in (4.9) implies that $\partial_t\boldsymbol{d}_h(0)\cdot\boldsymbol{t}^j|_\Sigma=\theta_{h,0}^j=0$. Now, taking $t\to 0$ in (4.2a)–(4.2b), (4.2c), and (4.2e) and using the above construction of the initial data, we conclude that $\boldsymbol{u}_h(0)=\boldsymbol{u}_{h,0}$, $p_{F,h}(0)=p_{F,h,0}$, $\boldsymbol{d}_h(0)=\boldsymbol{d}_{h,0}$, and $\varphi_h(0)=\varphi_{h,0}$.

We proceed with the stability bound (4.8a). Differentiating (4.2e) in time and taking $(\boldsymbol{v}_h,q_{F,h},\boldsymbol{w}_h,q_{P,h},\psi_h)=(\boldsymbol{u}_h,p_{F,h},\partial_t\boldsymbol{d}_h,p_{P,h},\varphi_h)$ in (4.2) gives

$$\begin{aligned} &2\mu_f\int_{\Omega_F}\boldsymbol{\epsilon}(\boldsymbol{u}_h):\boldsymbol{\epsilon}(\boldsymbol{u}_h)+\sum_{j=1}^{d-1}\langle\frac{\gamma\mu_f}{\sqrt{\kappa}}(\boldsymbol{u}_h-\partial_t\boldsymbol{d}_h)\cdot\boldsymbol{t}^j\,,(\boldsymbol{u}_h-\partial_t\boldsymbol{d}_h)\cdot\boldsymbol{t}^j\rangle_\Sigma+\frac{1}{2}\frac{\partial}{\partial t}2\mu_s\int_{\Omega_P}\boldsymbol{\epsilon}(\boldsymbol{d}_h):\boldsymbol{\epsilon}(\boldsymbol{d}_h)\\ &\quad+\frac{1}{2}\frac{\partial}{\partial t}C_0\int_{\Omega_P}p_{P,h}^2+\int_{\Omega_P}\frac{\kappa}{\mu_f}\nabla p_{P,h}\cdot\nabla p_{P,h}+\frac{1}{2}\frac{\partial}{\partial t}\frac{1}{\lambda}\int_{\Omega_P}(\alpha\,p_{P,h}-\varphi_h)^2\\ &\quad=\rho_f\int_{\Omega_F}\boldsymbol{g}\cdot\boldsymbol{u}_h+\rho_s\int_{\Omega_P}\boldsymbol{f}\cdot\partial_t\boldsymbol{d}_h+\rho_f\int_{\Omega_P}\frac{\kappa}{\mu_f}\boldsymbol{g}\cdot\nabla p_{P,h}-\rho_f\langle\frac{\kappa}{\mu_f}\boldsymbol{g}\cdot\boldsymbol{n},p_{P,h}\rangle_\Sigma.\end{aligned}\tag{4.11}$$

Integrating from 0 to $t\in(0,T]$, we obtain

$$2\mu_f\int_0^t\|\boldsymbol{\epsilon}(\boldsymbol{u}_h)\|_{\mathbf{L}^2(\Omega_F)}^2+\sum_{j=1}^{d-1}\gamma\mu_f\int_0^t\|\kappa^{-1/4}(\boldsymbol{u}_h-\partial_t\boldsymbol{d}_h)\cdot\boldsymbol{t}^j\|_{\mathbf{L}^2(\Sigma)}^2+\mu_s\|\boldsymbol{\epsilon}(\boldsymbol{d}_h)(t)\|_{\mathbf{L}^2(\Omega_P)}^2$$

$$
\begin{aligned}
&+\frac{C_0}{2}\|p_{P,h}(t)\|^2_{L^2(\Omega_P)}+\frac{1}{\mu_f}\int_0^t\|\kappa^{1/2}\nabla p_{P,h}\|^2_{L^2(\Omega_P)}+\frac{1}{2\lambda}\|(\alpha\, p_{P,h}-\varphi_h)(t)\|^2_{L^2(\Omega_P)}\\
&=\mu_s\|\boldsymbol{\epsilon}(\boldsymbol{d}_h)(0)\|^2_{\mathbf{L}^2(\Omega_P)}+\frac{C_0}{2}\|p_{P,h}(0)\|^2_{L^2(\Omega_P)}+\frac{1}{2\lambda}\|(\alpha\, p_{P,h}-\varphi_h)(0)\|^2_{L^2(\Omega_P)}\\
&\quad+\rho_f\int_0^t\int_{\Omega_F}\boldsymbol{g}\cdot\boldsymbol{u}_h-\rho_s\int_0^t\int_{\Omega_P}\partial_t\boldsymbol{f}\cdot\boldsymbol{d}_h+\rho_s\int_{\Omega_P}\boldsymbol{f}(t)\cdot\boldsymbol{d}_h(t)-\rho_s\int_{\Omega_P}\boldsymbol{f}(0)\cdot\boldsymbol{d}_h(0)\\
&\quad+\rho_f\int_0^t\int_{\Omega_P}\frac{\kappa}{\mu_f}\boldsymbol{g}\cdot\nabla p_{P,h}-\rho_f\int_0^t\langle\frac{\kappa}{\mu_f}\boldsymbol{g}\cdot\boldsymbol{n},p_{P,h}\rangle_\Sigma,
\end{aligned}
\tag{4.12}
$$

where we have integrated by parts in time the second term on the right-hand side in (4.11). Then, on the left-hand side we use Korn's inequality (4.5), the Poincaré inequality (4.4), and the permeability bound (4.7), whereas on the right-hand side we use the Cauchy-Schwarz inequality, the trace inequality (4.6), and Young's inequality, obtaining

$$
\begin{aligned}
&2\mu_f(c_K^F)^2\int_0^t\|\boldsymbol{u}_h\|^2_{\mathbf{H}^1(\Omega_F)}+\sum_{j=1}^{d-1}\frac{\gamma\mu_f}{\sqrt{\kappa_2}}\int_0^t\|(\boldsymbol{u}_h-\partial_t\boldsymbol{d}_h)\cdot\boldsymbol{t}^j\|^2_{\mathbf{L}^2(\Sigma)}+\mu_s(c_K^P)^2\|\boldsymbol{d}_h(t)\|^2_{\mathbf{H}^1(\Omega_P)}\\
&\quad+\frac{C_0}{2}\|p_{P,h}(t)\|^2_{L^2(\Omega_P)}+\frac{\kappa_1c_P^2}{\mu_f}\int_0^t\|p_{P,h}\|^2_{H^1(\Omega_P)}+\frac{1}{2\lambda}\|(\alpha\, p_{P,h}-\varphi_h)(t)\|^2_{L^2(\Omega_P)}\\
&\le\mu_s\|\boldsymbol{\epsilon}(\boldsymbol{d}_h)(0)\|^2_{\mathbf{L}^2(\Omega_P)}+\frac{C_0}{2}\|p_{P,h}(0)\|^2_{L^2(\Omega_P)}+\frac{1}{2\lambda}\|(\alpha\, p_{P,h}-\varphi_h)(0)\|^2_{L^2(\Omega_P)}\\
&\quad+\frac{\epsilon}{2}\left(\rho_f\int_0^t\|\boldsymbol{u}_h\|^2_{\mathbf{L}^2(\Omega_F)}+\rho_s\|\boldsymbol{d}_h(t)\|^2_{\mathbf{L}^2(\Omega_P)}+\frac{\rho_f\kappa_2}{\mu_f}((C_\Sigma^P)^2+1)\int_0^t\|p_{P,h}\|^2_{H^1(\Omega_P)}\right)\\
&\quad+\frac{1}{2\epsilon}\left(\rho_f\int_0^t\|\boldsymbol{g}\|^2_{\mathbf{L}^2(\Omega_F)}+\rho_s\|\boldsymbol{f}(t)\|^2_{\mathbf{L}^2(\Omega_P)}+\frac{\rho_f\kappa_2}{\mu_f}\int_0^t(\|\boldsymbol{g}\|^2_{\mathbf{L}^2(\Omega_P)}+\|\boldsymbol{g}\cdot\boldsymbol{n}\|^2_{L^2(\Sigma)})\right)\\
&\quad+\frac{\rho_s}{2}\int_0^t\|\boldsymbol{d}_h\|^2_{\mathbf{L}^2(\Omega_P)}+\frac{\rho_s}{2}\int_0^t\|\partial_t\boldsymbol{f}\|^2_{\mathbf{L}^2(\Omega_P)}+\frac{\rho_s}{2}\|\boldsymbol{d}_h(0)\|^2_{\mathbf{L}^2(\Omega_P)}+\frac{\rho_s}{2}\|\boldsymbol{f}(0)\|^2_{\mathbf{L}^2(\Omega_P)}.
\end{aligned}
\tag{4.13}
$$

Taking ϵ sufficiently small and employing Gronwall's inequality for the term $\frac{\rho_s}{2}\int_0^t\|\boldsymbol{d}_h\|^2_{\mathbf{L}^2(\Omega_P)}$, we obtain

$$
\begin{aligned}
&\int_0^t\|\boldsymbol{u}_h\|^2_{\mathbf{H}^1(\Omega_F)}+\sum_{j=1}^{d-1}\int_0^t\|(\boldsymbol{u}_h-\partial_t\boldsymbol{d}_h)\cdot\boldsymbol{t}^j\|^2_{\mathbf{L}^2(\Sigma)}+\|\boldsymbol{d}_h(t)\|^2_{\mathbf{H}^1(\Omega_P)}\\
&\qquad+\|p_{P,h}(t)\|^2_{L^2(\Omega_P)}+\int_0^t\|p_{P,h}\|^2_{H^1(\Omega_P)}+\frac{1}{\lambda}\|(\alpha\, p_{P,h}-\varphi_h)(t)\|^2_{L^2(\Omega_P)}\\
&\le C\Bigg(\int_0^t(\|\boldsymbol{g}\|^2_{\mathbf{L}^2(\Omega)}+\|\boldsymbol{g}\cdot\boldsymbol{n}\|^2_{L^2(\Sigma)})+\|\boldsymbol{f}(t)\|^2_{\mathbf{L}^2(\Omega_P)}\\
&\qquad+\|\boldsymbol{f}(0)\|^2_{\mathbf{L}^2(\Omega_P)}+\int_0^t\|\partial_t\boldsymbol{f}\|^2_{\mathbf{L}^2(\Omega_P)}+\|p_{P,0}\|^2_{H^1(\Omega_P)}\Bigg),
\end{aligned}
\tag{4.14}
$$

with a constant C independent of $\lambda_{\max}$. In the above inequality we have bounded the initial data terms by $C\|p_{P,0}\|^2_{H^1(\Omega_P)}$. This bound follows from the classical stability bound for the Stokes problem (4.2a)–(4.2b), which allows to obtain $\|\boldsymbol{u}_{h,0}\|_{\mathbf{H}^1(\Omega_F)}\le C\|p_{P,h,0}\|_{H^1(\Omega_P)}$; a stability bound for the saddle-point problem (4.2c), (4.2e) to obtain

$$
\|\boldsymbol{d}_{h,0}\|_{\mathbf{H}^1(\Omega_P)}+\|\varphi_{h,0}\|_{L^2(\Omega_p)}\le C(\|\boldsymbol{u}_{h,0}\|_{\mathbf{H}^1(\Omega_F)}+\|p_{P,h,0}\|_{H^1(\Omega_P)}),
$$

(cf. [45]), and the H^1-stability of the L^2-projection $\|p_{P,h,0}\|_{H^1(\Omega_P)} \leq C\|p_{P,0}\|_{H^1(\Omega_P)}$ (see, e.g., [14]).

Next we proceed with bounding $p_{F,h}$ and φ_h. The inf-sup condition (4.1a) together with (4.2a) give

$$\begin{aligned}
\beta_F\|p_{F,h}\|_{L^2(\Omega_F)} &\leq \sup_{\mathbf{0}\neq \boldsymbol{v}_h\in\mathbf{V}_h^\Sigma} \frac{b_1^F(\boldsymbol{v}_h,p_{F,h})}{\|\boldsymbol{v}_h\|_{\mathbf{H}^1(\Omega_F)}}\\
&= \sup_{\mathbf{0}\neq \boldsymbol{v}_h\in\mathbf{V}_h} \frac{-a_2^F(\boldsymbol{u}_h,\boldsymbol{v}_h)-b_2^\Sigma(\boldsymbol{v}_h,p_{P,h})-b_3^\Sigma(\boldsymbol{v}_h,\partial_t\boldsymbol{d}_h)+F^F(\boldsymbol{v}_h)}{\|\boldsymbol{v}_h\|_{\mathbf{H}^1(\Omega_F)}}\\
&\leq 2\mu_f\|\boldsymbol{u}_h\|_{\mathbf{H}^1(\Omega_F)}+\sum_{j=1}^{d-1}\frac{\gamma\mu_f C_\Sigma^F}{\sqrt{\kappa_1}}\|(\boldsymbol{u}_h-\partial_t\boldsymbol{d}_h)\cdot\boldsymbol{t}^j\|_{\mathbf{L}^2(\Sigma)}\\
&\quad + C_\Sigma^F C_\Sigma^P\|p_{P,h}\|_{H^1(\Omega_P)}+\rho_f\|\boldsymbol{g}\|_{\mathbf{L}^2(\Omega_F)},
\end{aligned}$$

implying

$$\int_0^t\|p_{F,h}\|^2_{L^2(\Omega_F)}\leq C\int_0^t\Big(\|\boldsymbol{u}_h\|^2_{\mathbf{H}^1(\Omega_F)}+\sum_{j=1}^{d-1}\|(\boldsymbol{u}_h-\partial_t\boldsymbol{d}_h)\cdot\boldsymbol{t}^j\|^2_{\mathbf{L}^2(\Sigma)}+\|p_{P,h}\|^2_{H^1(\Omega_P)}+\|\boldsymbol{g}\|^2_{\mathbf{L}^2(\Omega_F)}\Big). \quad (4.15)$$

Finally, using the inf-sup condition (4.1b) and (4.2c), we obtain

$$\begin{aligned}
\beta_P\|\varphi_h\|_{L^2(\Omega_P)} &\leq \sup_{\mathbf{0}\neq \boldsymbol{w}_h\in\mathbf{W}_h} \frac{b_1^P(\boldsymbol{w}_h,\varphi_h)}{\|\boldsymbol{w}_h\|_{\mathbf{H}^1(\Omega_P)}}\\
&= \sup_{\mathbf{0}\neq \boldsymbol{w}_h\in\mathbf{W}_h} \frac{-b_3^\Sigma(\boldsymbol{u}_h,\boldsymbol{w}_h)-b_4^\Sigma(\boldsymbol{w}_h,p_{P,h})-a_1^P(\boldsymbol{d}_h,\boldsymbol{w}_h)-a_2^\Sigma(\partial_t\boldsymbol{d}_h,\boldsymbol{w}_h)+F^P(\boldsymbol{w}_h)}{\|\boldsymbol{w}_h\|_{\mathbf{H}^1(\Omega_P)}}\\
&\leq (C_\Sigma^P)^2\|p_{P,h}\|_{H^1(\Omega_P)}+\sum_{j=1}^{d-1}\frac{\gamma\mu_f C_\Sigma^P}{\sqrt{\kappa_1}}\|(\boldsymbol{u}_h-\partial_t\boldsymbol{d}_h)\cdot\boldsymbol{t}^j\|_{\mathbf{L}^2(\Sigma)}\\
&\quad + 2\mu_s\|\boldsymbol{d}_h\|_{\mathbf{H}^1(\Omega_P)}+\rho_s\|\boldsymbol{f}\|_{\mathbf{L}^2(\Omega_P)},
\end{aligned}$$

yielding

$$\int_0^t\|\varphi_h\|^2_{L^2(\Omega_P)}\leq C\int_0^t\Big(\|p_{P,h}\|^2_{H^1(\Omega_P)}+\sum_{j=1}^{d-1}\|(\boldsymbol{u}_h-\partial_t\boldsymbol{d}_h)\cdot\boldsymbol{t}^j\|^2_{\mathbf{L}^2(\Sigma)}+\|\boldsymbol{d}_h\|^2_{\mathbf{H}^1(\Omega_P)}+\|\boldsymbol{f}\|^2_{\mathbf{L}^2(\Omega_P)}\Big). \quad (4.16)$$

Combining (4.14)–(4.16) and using Gronwall's inequality for the third term on the right-hand side in (4.16), we obtain (4.8a).

The above argument implies that the solution of (4.3) under the initial conditions $p_{P,h}(0)=p_{P,h,0}$, $\boldsymbol{d}_h(0)=\boldsymbol{d}_{h,0}$, and $\varphi_h(0)=\varphi_{h,0}$ is unique. In particular, taking $p_{P,h,0}=0$, $\boldsymbol{d}_{h,0}=\mathbf{0}$, $\varphi_{h,0}=0$, $\boldsymbol{g}=\mathbf{0}$, and $\boldsymbol{f}=\mathbf{0}$, (4.13) implies that (4.14) holds with right-hand side zero. Together with (4.15) and (4.16), this gives that all components of the solution are zero, therefore the solution is unique.

We next prove the higher regularity stability bound (4.8b). To that end, we differentiate in time (4.2a), (4.2c), and (4.2e) and take $(\boldsymbol{v}_h,q_{F,h},\boldsymbol{w}_h,q_{P,h},\psi_h)=(\boldsymbol{u}_h,\partial_t p_{F,h},\partial_t\boldsymbol{d}_h,\partial_t p_{P,h},\partial_t\varphi_h)$ in (4.2), obtaining

$$\frac{1}{2}\frac{\partial}{\partial t}2\mu_f\int_{\Omega_F}\boldsymbol{\epsilon}(\boldsymbol{u}_h):\boldsymbol{\epsilon}(\boldsymbol{u}_h)+\sum_{j=1}^{d-1}\frac{1}{2}\frac{\partial}{\partial t}\langle\frac{\gamma\mu_f}{\sqrt{\kappa}}(\boldsymbol{u}_h-\partial_t\boldsymbol{d}_h)\cdot\boldsymbol{t}^j,(\boldsymbol{u}_h-\partial_t\boldsymbol{d}_h)\cdot\boldsymbol{t}^j\rangle_\Sigma$$

$$+ 2\mu_s \int_{\Omega_P} \boldsymbol{\epsilon}(\partial_t \boldsymbol{d}_h) : \boldsymbol{\epsilon}(\partial_t \boldsymbol{d}_h) + C_0 \int_{\Omega_P} (\partial_t p_{P,h})^2 + \frac{1}{2}\frac{\partial}{\partial t} \int_{\Omega_P} \frac{\kappa}{\mu_f} \nabla p_{P,h} \cdot \nabla p_{P,h}$$
$$+ \frac{1}{\lambda} \int_{\Omega_P} (\alpha\, \partial_t p_{P,h} - \partial_t \varphi_h)^2 = \rho_s \int_{\Omega_P} \partial_t \boldsymbol{f} \cdot \partial_t \boldsymbol{d}_h + \rho_f \int_{\Omega_P} \frac{\kappa}{\mu_f} \boldsymbol{g} \cdot \partial_t \nabla p_{P,h} - \rho_f \langle \frac{\kappa}{\mu_f} \boldsymbol{g} \cdot \boldsymbol{n}, \partial_t p_{P,h} \rangle_\Sigma, \tag{4.17}$$

where we have used that $\partial_t \boldsymbol{g} = \boldsymbol{0}$. Integration from 0 to $t \in (0, T]$ gives

$$\mu_f \|\boldsymbol{\epsilon}(\boldsymbol{u}_h)(t)\|^2_{\mathbf{L}^2(\Omega_F)} + \sum_{j=1}^{d-1} \frac{1}{2} \gamma \mu_f \|\kappa^{-1/4} (\boldsymbol{u}_h - \partial_t \boldsymbol{d}_h) \cdot \boldsymbol{t}^j(t)\|^2_{\mathbf{L}^2(\Sigma)} + \mu_s \int_0^t \|\boldsymbol{\epsilon}(\partial_t \boldsymbol{d}_h)\|^2_{\mathbf{L}^2(\Omega_P)}$$
$$+ C_0 \int_0^t \|\partial_t p_{P,h}(t)\|^2_{L^2(\Omega_P)} + \frac{1}{2\mu_f} \|\kappa^{1/2} \nabla p_{P,h}(t)\|^2_{L^2(\Omega_P)} + \frac{1}{\lambda} \int_0^t \|\alpha\, \partial_t p_{P,h} - \partial_t \varphi_h\|^2_{L^2(\Omega_P)}$$
$$= \mu_f \|\boldsymbol{\epsilon}(\boldsymbol{u}_h)(0)\|^2_{\mathbf{L}^2(\Omega_F)} + \sum_{j=1}^{d-1} \frac{1}{2} \gamma \mu_f \|\kappa^{-1/4} (\boldsymbol{u}_h - \partial_t \boldsymbol{d}_h) \cdot \boldsymbol{t}^j(0)\|^2_{\mathbf{L}^2(\Sigma)} + \frac{1}{2\mu_f} \|\kappa^{1/2} \nabla p_{P,h}(0)\|^2_{L^2(\Omega_P)}$$
$$+ \rho_s \int_0^t \int_{\Omega_P} \partial_t \boldsymbol{f} \cdot \partial_t \boldsymbol{d}_h + \rho_f \int_{\Omega_P} \frac{\kappa}{\mu_f} \boldsymbol{g} \cdot (\nabla p_{P,h}(t) - \nabla p_{P,h}(0)) - \rho_f \langle \frac{\kappa}{\mu_f} \boldsymbol{g} \cdot \boldsymbol{n}, p_{P,h}(t) - p_{P,h}(0) \rangle_\Sigma,$$

where we have integrated by parts the last two terms in (4.17) and used that $\partial_t \boldsymbol{g} = \boldsymbol{0}$. Next, on the left-hand side we use Korn's inequality (4.5), the Poincaré inequality (4.4), and the permeability bound (4.7), while on the right-hand side we invoke Cauchy-Schwarz inequality, the trace inequality (4.6), and Young's inequality, yielding

$$\mu_f (c_K^F)^2 \|\boldsymbol{u}_h(t)\|^2_{\mathbf{H}^1(\Omega_F)} + \sum_{j=1}^{d-1} \frac{1}{2} \frac{\gamma \mu_f}{\sqrt{\kappa_2}} \|(\boldsymbol{u}_h - \partial_t \boldsymbol{d}_h) \cdot \boldsymbol{t}^j(t)\|^2_{\mathbf{L}^2(\Sigma)} + \mu_s (c_K^P)^2 \int_0^t \|\partial_t \boldsymbol{d}_h\|^2_{\mathbf{H}^1(\Omega_P)}$$
$$+ C_0 \int_0^t \|\partial_t p_{P,h}(t)\|^2_{L^2(\Omega_P)} + \frac{\kappa_1 c_P^2}{2\mu_f} \|p_{P,h}(t)\|^2_{H^1(\Omega_P)} + \frac{1}{\lambda} \int_0^t \|\alpha\, \partial_t p_{P,h} - \partial_t \varphi_h\|^2_{L^2(\Omega_P)}$$
$$\leq \mu_f \|\boldsymbol{\epsilon}(\boldsymbol{u}_h)(0)\|^2_{\mathbf{L}^2(\Omega_F)} + \sum_{j=1}^{d-1} \frac{1}{2} \frac{\gamma \mu_f}{\sqrt{\kappa_1}} \|(\boldsymbol{u}_h - \partial_t \boldsymbol{d}_h) \cdot \boldsymbol{t}^j(0)\|^2_{\mathbf{L}^2(\Sigma)} + \frac{\kappa_2}{2\mu_f} \|\nabla p_{P,h}(0)\|^2_{L^2(\Omega_P)}$$
$$+ \frac{\epsilon}{2} \left(\rho_s \int_0^t \|\partial_t \boldsymbol{d}_h\|^2_{\mathbf{L}^2(\Omega_P)} + \frac{\rho_f \kappa_2}{\mu_f} ((C_\Sigma^P)^2 + 1)(\|p_{P,h}(0)\|^2_{H^1(\Omega_P)} + \|p_{P,h}(t)\|^2_{H^1(\Omega_P)}) \right)$$
$$+ \frac{1}{2\epsilon} \left(\rho_s \int_0^t \|\partial_t \boldsymbol{f}\|^2_{\mathbf{L}^2(\Omega_P)} + \frac{\rho_f \kappa_2}{\mu_f} (\|\boldsymbol{g}\|^2_{\mathbf{L}^2(\Omega_P)} + \|\boldsymbol{g} \cdot \boldsymbol{n}\|^2_{L^2(\Sigma)}) \right).$$

In addition, bounding the initial data terms as in (4.14) and taking ϵ sufficiently small, we can assert that

$$\|\boldsymbol{u}_h(t)\|^2_{\mathbf{H}^1(\Omega_F)} + \sum_{j=1}^{d-1} \|(\boldsymbol{u}_h - \partial_t \boldsymbol{d}_h) \cdot \boldsymbol{t}^j(t)\|^2_{\mathbf{L}^2(\Sigma)} + \int_0^t \|\partial_t \boldsymbol{d}_h\|^2_{\mathbf{H}^1(\Omega_P)}$$
$$+ \int_0^t \|\partial_t p_{P,h}(t)\|^2_{L^2(\Omega_P)} + \|p_{P,h}(t)\|^2_{H^1(\Omega_P)} + \frac{1}{\lambda} \int_0^t \|\alpha\, \partial_t p_{P,h} - \partial_t \varphi_h\|^2_{L^2(\Omega_P)}$$
$$\leq C \left(\int_0^t \|\partial_t \boldsymbol{f}\|^2_{\mathbf{L}^2(\Omega_P)} + \|\boldsymbol{g}\|^2_{\mathbf{L}^2(\Omega_P)} + \|\boldsymbol{g} \cdot \boldsymbol{n}\|^2_{L^2(\Sigma)} + \|p_{P,0}\|^2_{H^1(\Omega_P)} \right), \tag{4.18}$$

with a constant C independent of $\lambda_{\max}$. Next, using the inf-sup conditions (4.1a) and (4.1b), and proceeding similarly to the derivations of (4.15) and (4.16), we obtain

$$\|p_{F,h}(t)\|^2_{L^2(\Omega_F)} \leq C\Big(\|\boldsymbol{u}_h(t)\|^2_{\mathbf{H}^1(\Omega_F)} + \sum_{j=1}^{d-1} \|(\boldsymbol{u}_h - \partial_t \boldsymbol{d}_h)\cdot \boldsymbol{t}^j(t)\|^2_{\mathbf{L}^2(\Sigma)} + \|p_{P,h}(t)\|^2_{H^1(\Omega_P)} + \|\boldsymbol{g}\|^2_{\mathbf{L}^2(\Omega_F)}\Big),$$

and

$$\|\varphi_h(t)\|^2_{L^2(\Omega_P)} \leq C\Big(\|p_{P,h}(t)\|^2_{H^1(\Omega_P)} + \sum_{j=1}^{d-1} \|(\boldsymbol{u}_h - \partial_t \boldsymbol{d}_h)\cdot \boldsymbol{t}^j(t)\|^2_{\mathbf{L}^2(\Sigma)} + \|\boldsymbol{d}_h(t)\|^2_{\mathbf{H}^1(\Omega_P)} + \|\boldsymbol{f}(t)\|^2_{\mathbf{L}^2(\Omega_P)}\Big). \tag{4.19}$$

Finally, combining (4.18)–(4.19) and employing (4.8a) for the control of $\|\boldsymbol{d}_h(t)\|_{\mathbf{H}^1(\Omega_P)}$, we obtain the second bound (4.8b). □

Remark 4.1. *We emphasise that, even though initial data was constructed for all variables, the initial value problem for (4.3) involves initial conditions only for $p_{P,h}$, $\boldsymbol{d}_h$, and φ_h.*

4.3. Existence, uniqueness, and stability of the weak solution

Theorem 4.2. *For each $\boldsymbol{f} \in H^1(0,T;\mathbf{L}^2(\Omega_P))$ and $p_{P,0} \in H^1_\star(\Omega_p)$, there exist initial data $\boldsymbol{u}_0 \in \mathbf{H}^1_\star(\Omega_F)$, $p_{F,0} \in L^2(\Omega_F)$, $\boldsymbol{d}_0 \in \mathbf{H}^1_\star(\Omega_P)$, and $\varphi_0 \in L^2(\Omega_P)$ such that the weak formulation (3.1) with $a_1^F = 0$, $c^F = 0$, and $\tilde{\alpha} = 1$, complemented with the initial conditions $p_P(0) = p_{P,0}$, $\boldsymbol{d}(0) = \boldsymbol{d}_0$, and $\varphi(0) = \varphi_0$, has a unique solution satisfying*

$$\begin{aligned}
&\|\boldsymbol{u}\|_{L^2(0,T;\mathbf{H}^1(\Omega_F))} + \|p_F\|_{L^2(0,T;L^2(\Omega_F))} + \|\boldsymbol{d}\|_{L^\infty(0,T;\mathbf{H}^1(\Omega_P))} \\
&\quad + \sum_{j=1}^{d-1} \|(\boldsymbol{u} - \partial_t \boldsymbol{d})\cdot \boldsymbol{t}^j\|_{L^2(0,T;L^2(\Sigma))} + \|p_P\|_{L^\infty(0,T;L^2(\Omega_P))} + \|p_P\|_{L^2(0,T;H^1(\Omega_P))} \\
&\quad + \|\varphi\|_{L^2(0,T;L^2(\Omega_P))} + \frac{1}{\sqrt{\lambda}}\|\alpha\, p_P - \varphi\|_{L^\infty(0,T;L^2(\Omega_P))} \\
&\leq C\left(\|\boldsymbol{g}\|_{L^2(0,T;\mathbf{L}^2(\Omega))} + \|\boldsymbol{g}\cdot\boldsymbol{n}\|_{L^2(0,T;L^2(\Sigma))} + \|\boldsymbol{f}\|_{H^1(0,T;\mathbf{L}^2(\Omega_P))} + \|p_{P,0}\|_{H^1(\Omega_P)}\right),
\end{aligned} \tag{4.20a}$$

and

$$\begin{aligned}
&\|\boldsymbol{u}\|_{L^\infty(0,T;\mathbf{H}^1(\Omega_F))} + \|p_F\|_{L^\infty(0,T;L^2(\Omega_F))} + \|\partial_t \boldsymbol{d}\|_{L^2(0,T;\mathbf{H}^1(\Omega_P))} \\
&\quad + \sum_{j=1}^{d-1} \|(\boldsymbol{u} - \partial_t \boldsymbol{d})\cdot \boldsymbol{t}^j\|_{L^\infty(0,T;L^2(\Sigma))} + \|\partial_t p_P\|_{L^2(0,T;L^2(\Omega_P))} + \|p_P\|_{L^\infty(0,T;H^1(\Omega_P))} \\
&\quad + \|\varphi\|_{L^\infty(0,T;L^2(\Omega_P))} + \frac{1}{\sqrt{\lambda}}\|\alpha\, \partial_t p_P - \partial_t \varphi\|_{L^2(0,T;L^2(\Omega_P))} \\
&\leq C\left(\|\boldsymbol{g}\|_{L^2(0,T;\mathbf{L}^2(\Omega))} + \|\boldsymbol{g}\cdot\boldsymbol{n}\|_{L^2(0,T;L^2(\Sigma))} + \|\boldsymbol{f}\|_{H^1(0,T;\mathbf{L}^2(\Omega_P))} + \|p_{P,0}\|_{H^1(\Omega_P)}\right),
\end{aligned} \tag{4.20b}$$

with a constant C independent of $\lambda_{\max}$.

Proof. From Theorem 4.1, there exists an infinite sequence $\{(\boldsymbol{u}_h, p_{F,h}, \boldsymbol{d}_h, p_{P,h}, \varphi_h)\}_{h>0}$ satisfying (4.3) for each h such that $\{\boldsymbol{u}_h\}_{h>0}$ is bounded in $L^2(0,T;\mathbf{H}^1(\Omega_F))$, $\{p_{F,h}\}_{h>0}$ is bounded in $L^2(0,T;L^2(\Omega_F))$, $\{\boldsymbol{d}_h\}_{h>0}$ is bounded in $H^1(0,T;\mathbf{H}^1(\Omega_P))$, the sequence $\{p_{P,h}\}_{h>0}$ is bounded in $H^1(0,T;L^2(\Omega_P))$, as

well as in $L^2(0,T;H^1(\Omega_P))$, and the sequence $\{\varphi_h\}_{h>0}$ is bounded in $H^1(0,T;L^2(\Omega_P))$. Therefore there exist weakly convergent subsequences, denoted in the same way, such that

$$\boldsymbol{u}_h \rightharpoonup \boldsymbol{u} \text{ in } L^2(0,T;\mathbf{H}^1(\Omega_F)), \quad p_{F,h} \rightharpoonup p_F \text{ in } L^2(0,T;L^2(\Omega_F)),$$
$$\boldsymbol{d}_h \rightharpoonup \boldsymbol{d} \text{ in } H^1(0,T;\mathbf{H}^1(\Omega_P)),$$
$$p_{P,h} \rightharpoonup p_P \text{ in } H^1(0,T;L^2(\Omega_P)) \cap L^2(0,T;H^1(\Omega_P)), \quad \varphi_h \rightharpoonup \varphi \text{ in } H^1(0,T;L^2(\Omega_P)).$$

Next, we fix a set of test functions $(\boldsymbol{v}_h, q_{F,h}, \boldsymbol{w}_h, q_{P,h}, \psi_h) \in C^0(0,T;\mathbf{V}_h \times \mathrm{Q}_h^F \times \mathbf{W}_h \times \mathrm{Q}_h^P \times \mathrm{Z}_h)$ in (4.2), integrate it in time from 0 to T, and take $h \to 0$. Since all bilinear forms and linear functionals are continuous, cf. Lemma 4.1, we conclude that $(\boldsymbol{u}, p_F, \boldsymbol{d}, p_P, \varphi)$ satisfy the time-integrated version of (3.1) with this choice of test functions. Finally, since the space $C^0(0,T;\mathbf{V}_h \times \mathrm{Q}_h^F \times \mathbf{W}_h \times \mathrm{Q}_h^P \times \mathrm{Z}_h)$ is dense in $L^2(0,T;\mathbf{H}^1_\star(\Omega_F) \times L^2(\Omega_F) \times \mathbf{H}^1_\star(\Omega_P) \times H^1_\star(\Omega_P) \times L^2(\Omega_P))$, we conclude that (3.1) holds for a.e. $t \in (0,T)$.

It remains to handle the initial conditions. First, taking $h \to 0$ in $p_{P,h}(0) = p_{P,h,0}$ gives $p_P(0) = p_{P,0}$. We further note that the control of the terms $\|(\boldsymbol{u}_h - \partial_t \boldsymbol{d}_h)\cdot \boldsymbol{t}^j\|_{L^\infty(0,T;L^2(\Sigma))}$ and $\|\boldsymbol{u}_h\|_{L^\infty(0,T;\mathbf{H}^1(\Omega_F))}$ in (4.8b) implies that for all $t \in [0,T]$, $\partial_t \boldsymbol{d}_h(t)\cdot\boldsymbol{t}^j \rightharpoonup \partial_t \boldsymbol{d}(t)\cdot\boldsymbol{t}^j$ in $L^2(\Sigma)$. Taking $t = 0$ and $h \to 0$ in (4.9) and using that $\partial_t \boldsymbol{d}_h(0)\cdot\boldsymbol{t}^j = 0$ on Σ, we conclude that $\partial_t \boldsymbol{d}(0)\cdot\boldsymbol{t}^j = 0$ on Σ. Next, the stability of the Stokes and elasticity problems for the initial data in the proof of Theorem 4.1 implies that there exist weakly convergent subsequences such that

$$\boldsymbol{u}_{h,0} \rightharpoonup \boldsymbol{u}_0 \text{ in } \mathbf{H}^1(\Omega_F), \quad p_{F,h,0} \rightharpoonup p_{F,0} \text{ in } L^2(\Omega_F), \quad \boldsymbol{d}_{h,0} \rightharpoonup \boldsymbol{d}_0 \text{ in } \mathbf{H}^1(\Omega_P), \quad \varphi_{h,0} \rightharpoonup \varphi_0 \text{ in } L^2(\Omega_P).$$

Then, taking $t \to 0$ in (3.1a)–(3.1b), (3.1c), and (3.1e) and using that the initial data satisfies the same equations, we conclude that $\boldsymbol{u}(0) = \boldsymbol{u}_0$, $p_F(0) = p_{F,0}$, $\boldsymbol{d}(0) = \boldsymbol{d}_0$, and $\varphi(0) = \varphi_0$.

Finally, the uniqueness of the solution under the initial conditions $p_P(0) = p_{P,0}$, $\boldsymbol{d}(0) = \boldsymbol{d}_0$, $\varphi(0) = \varphi_0$, and the stability bounds (4.20a) and (4.20b), follow in the same way as in the proof of Theorem 4.1. □

5. Fully discrete scheme

We apply a time discretisation to (4.2) using backward Euler's method with fixed time step $\Delta t = T/N$. Let $t_n = n\Delta t$, $n = 0,\dots,N$, be the discrete times. Starting from the discrete initial data constructed in the proof of Theorem 4.1, at each time iteration $n = 1,\dots,N$ we look for $(\boldsymbol{u}_h^n, p_{F,h}^n, \boldsymbol{d}_h^n, p_{P,h}^n, \varphi_h^n) \in \mathbf{V}_h \times \mathrm{Q}_h^F \times \mathbf{W}_h \times \mathrm{Q}_h^P \times \mathrm{Z}_h =: \mathbf{H}_h$ such that

$$a_2^F(\boldsymbol{u}_h^n, \boldsymbol{v}_h) + b_1^F(\boldsymbol{v}_h, p_{F,h}^n) + b_2^\Sigma(\boldsymbol{v}_h, p_{P,h}^n) + b_3^\Sigma(\boldsymbol{v}_h, \partial_t^n \boldsymbol{d}_h) = F^{F,n}(\boldsymbol{v}_h) \qquad \forall \boldsymbol{v}_h \in \mathbf{V}_h, \tag{5.1a}$$
$$-b_1^F(\boldsymbol{u}_h^n, q_{F,h}) = 0 \qquad \forall q_{F,h} \in \mathrm{Q}_h^F, \tag{5.1b}$$
$$b_3^\Sigma(\boldsymbol{u}_h^n, \boldsymbol{w}_h) + b_4^\Sigma(\boldsymbol{w}_h, p_{P,h}^n) + a_1^P(\boldsymbol{d}_h^n, \boldsymbol{w}_h) + a_2^\Sigma(\partial_t^n \boldsymbol{d}_h, \boldsymbol{w}_h) + b_1^P(\boldsymbol{w}_h, \varphi_h^n) = F^P(\boldsymbol{w}_h) \qquad \forall \boldsymbol{w}_h \in \mathbf{W}_h, \tag{5.1c}$$
$$-b_2^\Sigma(\boldsymbol{u}_h^n, q_{P,h}) - b_4^\Sigma(\partial_t^n \boldsymbol{d}_h, q_{P,h}) + a_3^P(\partial_t^n p_{P,h}, q_{P,h}) + a_4^P(p_{P,h}^n, q_{P,h}) - b_2^P(\partial_t^n \varphi_h, q_{P,h}) = G^n(q_{P,h}) \qquad \forall q_{P,h} \in \mathrm{Q}_h^P, \tag{5.1d}$$
$$-b_1^P(\boldsymbol{d}_h^n, \psi_h) - b_2^P(\psi_h, p_{P,h}^n) + a_5^P(\varphi_h^n, \psi_h) = 0 \qquad \forall \psi_h \in \mathrm{Z}_h, \tag{5.1e}$$

where, for a generic scalar or vector field f, we set $f^n := f(t_n)$ and $\partial_t^n f := \frac{1}{\Delta t}(f^n - f^{n-1})$. For convenience we also define the global discrete time derivative $\tilde{\partial}_t f$ such that $(\tilde{\partial}_t f)^n := \partial_t^n f$ for $n =$

$1,\dots,N$. The method requires solving at each time step the algebraic system

$$\left[\begin{array}{cc:ccc} \mathcal{A}_2^F & (\mathcal{B}_1^F)' & \frac{1}{\Delta t}(\mathcal{B}_3^\Sigma)' & (\mathcal{B}_2^\Sigma)' & \mathbf{0} \\ -\mathcal{B}_1^F & \mathbf{0} & \mathbf{0} & \mathbf{0} & \mathbf{0} \\ \hdashline \mathcal{B}_3^\Sigma & \mathbf{0} & \mathcal{A}_1^P + \frac{1}{\Delta t}\mathcal{A}_2^\Sigma & (\mathcal{B}_4^\Sigma)' & (\mathcal{B}_1^P)' \\ -\mathcal{B}_2^\Sigma & \mathbf{0} & -\frac{1}{\Delta t}\mathcal{B}_4^\Sigma & \frac{1}{\Delta t}\mathcal{A}_3^P + \mathcal{A}_4^P & -\frac{1}{\Delta t}(\mathcal{B}_2^P)' \\ \mathbf{0} & \mathbf{0} & -\mathcal{B}_1^P & -\mathcal{B}_2^P & \mathcal{A}_5^P \end{array}\right] \left[\begin{array}{c} \boldsymbol{u}_h^n \\ p_{F,h}^n \\ \boldsymbol{d}_h^n \\ p_{P,h}^n \\ \varphi_h^n \end{array}\right] = \left[\begin{array}{c} \tilde{\mathcal{F}}^{F,n} \\ \mathbf{0} \\ \tilde{\mathcal{F}}^{P,n} \\ \tilde{\mathcal{G}}^n \\ \mathbf{0} \end{array}\right], \tag{5.2}$$

where the tilde-notation on the right-hand side vectors indicate that they also receive contributions from the backward Euler time-discretisation.

Theorem 5.1. *The fully discrete method* (5.2) *has a unique solution.*

Proof. Consider the matrix obtained from the matrix in (5.2) by scaling the third and fifth rows by $\frac{1}{\Delta t}$. It has the same structure as the matrix $\mathcal{N}+\mathcal{M}$ that appears in the proof of Theorem 4.1, which is shown to be nonsingular. Therefore the scaled matrix is nonsingular, and so is the matrix in (5.2). □

5.1. Error estimates for the fully discrete scheme

We proceed with the error analysis for the fully discrete scheme. We will make use of the discrete space-time norms for $f : t_n \to \mathrm{V}$, $n = 1,\dots,N$,

$$\|f\|^2_{l^2(0,T;\mathrm{V})} := \sum_{n=1}^{N} \Delta t \|f^n\|^2_{\mathrm{V}}, \quad \|f\|_{l^\infty(0,T;\mathrm{V})} := \max_{n=1,\dots,N} \|f^n\|_{\mathrm{V}},$$

In addition, we consider finite-dimensional subspaces of continuous and piecewise polynomials of generic degrees

$$k_{\boldsymbol{v}}, k_{\boldsymbol{w}}, k_{q_P} \geq 1, \quad k_{q_F}, k_z \geq 0, \quad \text{for the spaces} \quad \mathbf{V}_h, \mathbf{W}_h, \mathrm{Q}_h^P, \mathrm{Q}_h^F, \mathrm{Z}_h, \tag{5.3}$$

respectively.

Let $I^{\mathbf{V}} : \mathbf{H}^1_\star(\Omega_F) \to \mathbf{V}_h$, $I^{\mathbf{W}} : \mathbf{H}^1_\star(\Omega_P) \to \mathbf{W}_h$, and $I^{\mathrm{Q}^P} : H^1_\star(\Omega_P) \to \mathrm{Q}_h^P$ be the Scott-Zhang interpolants [48]. In addition, let $I^{\mathrm{Q}^F} : L^2(\Omega_F) \to \mathrm{Q}_h^F$ and $I^{\mathrm{Z}} : L^2(\Omega_P) \to \mathrm{Z}_h$ be the L^2-orthogonal projections. These operators, alongside the polynomial degrees (5.3) have the approximation properties (see, e.g., [48, 22])

$$\|\boldsymbol{v} - I^{\mathbf{V}}\boldsymbol{v}\|_{\mathbf{H}^s(\Omega_F)} \leq Ch^{r_{\boldsymbol{v}}-s}\|\boldsymbol{v}\|_{\mathbf{H}^{r_{\boldsymbol{v}}}(\Omega_F)}, \qquad 1 \leq r_{\boldsymbol{v}} \leq k_{\boldsymbol{v}}+1,\ 0 \leq s \leq 1, \tag{5.4a}$$

$$\|q_F - I^{\mathrm{Q}^F} q_F\|_{L^2(\Omega_P)} \leq Ch^{r_{q_F}}\|q_F\|_{H^{r_{q_F}}(\Omega_F)}, \qquad 0 \leq r_{q_F} \leq k_{q_F}+1, \tag{5.4b}$$

$$\|\boldsymbol{w} - I^{\mathbf{W}}\boldsymbol{w}\|_{\mathbf{H}^s(\Omega_P)} \leq Ch^{r_{\boldsymbol{w}}-s}\|\boldsymbol{w}\|_{\mathbf{H}^{r_{\boldsymbol{w}}}(\Omega_P)}, \qquad 1 \leq r_{\boldsymbol{w}} \leq k_{\boldsymbol{w}}+1,\ 0 \leq s \leq 1, \tag{5.4c}$$

$$\|q_P - I^{\mathrm{Q}^P} q_P\|_{H^s(\Omega_P)} \leq Ch^{r_{q_P}-s}\|q_P\|_{H^{r_{q_P}}(\Omega_P)}, \qquad 1 \leq r_{q_P} \leq k_{q_P}+1,\ 0 \leq s \leq 1, \tag{5.4d}$$

$$\|\psi - I^{\mathrm{Z}}\psi\|_{L^2(\Omega_P)} \leq Ch^{r_z}\|\psi\|_{H^{r_z}(\Omega_P)}, \qquad 0 \leq r_z \leq k_z+1. \tag{5.4e}$$

Theorem 5.2. *Assume that the weak solution of (3.1) is sufficiently smooth. Then, for the fully discrete solution (5.1), there exists a constant C independent of $\lambda_{\max}$, h, and Δt, such that*

$$\begin{aligned}
&\|\boldsymbol{u}-\boldsymbol{u}_h\|_{l^2(0,T;\mathbf{H}^1(\Omega_F))}+\|p_F-p_{F,h}\|_{l^2(0,T;L^2(\Omega_F))}+\|\boldsymbol{d}-\boldsymbol{d}_h\|_{l^\infty(0,T;\mathbf{H}^1(\Omega_P))}\\
&\quad+\sum_{j=1}^{d-1}\|(\boldsymbol{u}-\tilde{\partial}_t\boldsymbol{d}_h)\cdot\boldsymbol{t}^j\|_{l^2(0,T;L^2(\Sigma))}+\|p_P-p_{P,h}\|_{l^\infty(0,T;L^2(\Omega_P))}+\|p_P-p_{P,h}\|_{l^2(0,T;H^1(\Omega_P))}\\
&\quad+\|\varphi-\varphi_h\|_{l^2(0,T;L^2(\Omega_P))}+\frac{1}{\sqrt{\lambda}}\|(\alpha\,p_P-\varphi)-(\alpha\,p_{P,h}-\varphi_h)\|_{l^\infty(0,T;L^2(\Omega_P))}\\
&\le C\Big(h^{r_{\boldsymbol{v}}}\|\boldsymbol{u}\|_{H^1(0,T;\mathbf{H}^{r_{\boldsymbol{v}}+1}(\Omega_F))}+h^{r_{q_F}}\|p_F\|_{H^1(0,T;H^{r_{q_F}}(\Omega_F))}+h^{r_{\boldsymbol{w}}}\|\boldsymbol{d}\|_{W^{2,\infty}(0,T;\mathbf{H}^{r_{\boldsymbol{w}}+1}(\Omega_P))}\\
&\qquad+h^{r_{q_P}}\|p_P\|_{H^1(0,T;H^{r_{q_P}+1}(\Omega_P))}+h^{r_z}\|\varphi\|_{H^1(0,T;H^{r_z}(\Omega_P))}\\
&\qquad+\Delta t\big(\|\boldsymbol{d}\|_{H^3(0,T;\mathbf{L}^2(\Sigma))}+\|p_P\|_{H^2(0,T;L^2(\Omega_P)}+\|\varphi\|_{H^2(0,T;L^2(\Omega_P))}\big)\Big),
\end{aligned}\tag{5.5}$$

with $1\le r_{\boldsymbol{v}}\le k_{\boldsymbol{v}}$, $0\le r_{q_F}\le k_{q_F}+1$, $1\le r_{\boldsymbol{w}}\le k_{\boldsymbol{w}}$, $1\le r_{q_P}\le k_{q_P}$, *and* $0\le r_z\le k_z+1$.

Proof. We decompose the numerical errors into approximation and discretisation components:

$$\begin{aligned}
\boldsymbol{u}-\boldsymbol{u}_h&=(\boldsymbol{u}-I^{\mathbf{V}}\boldsymbol{u})+(I^{\mathbf{V}}\boldsymbol{u}-\boldsymbol{u}_h)=:e_{\boldsymbol{u},I}+e_{\boldsymbol{u},h},\\
p_F-p_{F,h}&=(p_F-I^{\mathrm{Q}^F}p_F)+(I^{\mathrm{Q}^F}p_F-p_{F,h})=:e_{p_F,I}+e_{p_F,h},\\
\boldsymbol{d}-\boldsymbol{d}_h&=(\boldsymbol{d}-I^{\mathbf{W}}\boldsymbol{d})+(I^{\mathbf{W}}\boldsymbol{d}-\boldsymbol{d}_h)=:e_{\boldsymbol{d},I}+e_{\boldsymbol{d},h},\\
p_P-p_{P,h}&=(p_P-I^{\mathrm{Q}^P}p_P)+(I^{\mathrm{Q}^P}p_P-p_{P,h})=:e_{p_P,I}+e_{p_P,h},\\
\varphi-\varphi_h&=(\varphi-I^{\mathrm{Z}}\varphi)+(I^{\mathrm{Z}}\varphi-\varphi_h)=:e_{\varphi,I}+e_{\varphi,h}.
\end{aligned}$$

Denote the time discretisation errors as $r_\phi^n:=\phi(t_n)-\partial_t^n\phi$, for $\phi\in\{\boldsymbol{d},p_P,\varphi\}$. Subtracting (5.1) from (3.1), we obtain the error system

$$\begin{aligned}
&a_2^F(e^n_{\boldsymbol{u},h},\boldsymbol{v}_h)+b_1^F(\boldsymbol{v}_h,e^n_{p_F,h})+b_2^\Sigma(\boldsymbol{v}_h,e^n_{p_P,h})+b_3^\Sigma(\boldsymbol{v}_h,\partial_t^n e_{\boldsymbol{d},h})\\
&\quad=-a_2^F(e^n_{\boldsymbol{u},I},\boldsymbol{v}_h)-b_1^F(\boldsymbol{v}_h,e^n_{p_F,I})-b_2^\Sigma(\boldsymbol{v}_h,e^n_{p_P,I})-b_3^\Sigma(\boldsymbol{v}_h,\partial_t^n e_{\boldsymbol{d},I})-b_3^\Sigma(\boldsymbol{v}_h,r^n_{\boldsymbol{d}}),&(5.6a)\\
&-b_1^F(e^n_{\boldsymbol{u},h},q_{F,h})=b_1^F(e^n_{\boldsymbol{u},I},q_{F,h}),&(5.6b)\\
&b_3^\Sigma(e^n_{\boldsymbol{u},h},\boldsymbol{w}_h)+b_4^\Sigma(\boldsymbol{w}_h,e^n_{p_P,h})+a_1^P(e^n_{\boldsymbol{d},h},\boldsymbol{w}_h)+a_2^\Sigma(\partial_t^n e_{\boldsymbol{d},h},\boldsymbol{w}_h)+b_1^P(\boldsymbol{w}_h,e^n_{\varphi,h})=-b_3^\Sigma(e^n_{\boldsymbol{u},I},\boldsymbol{w}_h)\\
&\quad-b_4^\Sigma(\boldsymbol{w}_h,e^n_{p_P,I})-a_1^P(e^n_{\boldsymbol{d},I},\boldsymbol{w}_h)-a_2^\Sigma(\partial_t^n e_{\boldsymbol{d},I},\boldsymbol{w}_h)-b_1^P(\boldsymbol{w}_h,e^n_{\varphi,I})-a_2^\Sigma(r^n_{\boldsymbol{d}},\boldsymbol{w}_h),&(5.6c)\\
&-b_2^\Sigma(e^n_{\boldsymbol{u},h},q_{P,h})-b_4^\Sigma(\partial_t^n e_{\boldsymbol{d},h},q_{P,h})+a_3^P(\partial_t^n e_{p_P,h},q_{P,h})+a_4^P(e^n_{p_P,h},q_{P,h})-b_2^P(\partial_t^n e_{\varphi,h},q_{P,h})\\
&\quad=b_2^\Sigma(e^n_{\boldsymbol{u},I},q_{P,h})+b_4^\Sigma(\partial_t^n e_{\boldsymbol{d},I},q_{P,h})-a_3^P(\partial_t^n e_{p_P,I},q_{P,h})-a_4^P(e^n_{p_P,I},q_{P,h})\\
&\quad+b_2^P(\partial_t^n e_{\varphi,I},q_{P,h})-a_3^P(r^n_{p_P},q_{P,h})-b_2^P(r^n_{\varphi},q_{P,h}),&(5.6d)\\
&-b_1^P(\partial_t^n e_{\boldsymbol{d},h},\psi_h)-b_2^P(\psi_h,\partial_t^n e_{p_P,h})+a_5^P(\partial_t^n e_{\varphi,h},\psi_h)=b_1^P(\partial_t^n e_{\boldsymbol{d},I},\psi_h)+b_2^P(\psi_h,\partial_t^n e_{p_P,I}).&(5.6e)
\end{aligned}$$

Equation (5.6e) has been obtained by taking the divided difference of the error equation at t_n and t_{n-1} for $n=1,\dots,N$, using that it is satisfied by the initial data. We also used the orthogonality property of I^{Z} to conclude that $a_5^P(\partial_t^n e_{\varphi,I},\psi_h)=0$. Now, taking $(\boldsymbol{v}_h,q_{F,h},\boldsymbol{w}_h,q_{P,h},\psi_h)=(e^n_{\boldsymbol{u},h},e^n_{p_F,h},\partial_t^n e_{\boldsymbol{d},h},e^n_{p_P,h},e^n_{\varphi,h})$ in (5.6), summing the equations, and using the identity

$$(\partial_t^n\phi)\phi^n=\frac{1}{2}\partial_t^n(\phi^2)+\frac{1}{2}\Delta t(\partial_t^n\phi)^2,$$

results in

$$
\begin{aligned}
&2\mu_f \int_{\Omega_F} \boldsymbol{\epsilon}(e^n_{\boldsymbol{u},h}) : \boldsymbol{\epsilon}(e^n_{\boldsymbol{u},h}) + \sum_{j=1}^{d-1} \langle \frac{\gamma \mu_f}{\sqrt{\kappa}} (e^n_{\boldsymbol{u},h} - \partial_t^n e_{\boldsymbol{d},h}) \cdot \boldsymbol{t}^j \, , (e^n_{\boldsymbol{u},h} - \partial_t^n e_{\boldsymbol{d},h}) \cdot \boldsymbol{t}^j \rangle_\Sigma \\
&\quad + \frac{1}{2} \partial_t^n 2\mu_s \int_{\Omega_P} \boldsymbol{\epsilon}(e_{\boldsymbol{d},h}) : \boldsymbol{\epsilon}(e_{\boldsymbol{d},h}) + \frac{1}{2} \Delta t \, 2\mu_s \int_{\Omega_P} \partial_t^n \boldsymbol{\epsilon}(e_{\boldsymbol{d},h}) : \partial_t^n \boldsymbol{\epsilon}(e_{\boldsymbol{d},h}) \\
&\quad + \frac{1}{2} \partial_t^n C_0 \int_{\Omega_P} (e_{p_P,h})^2 + \frac{1}{2} \Delta t C_0 \int_{\Omega_P} (\partial_t^n e_{p_P,h})^2 + \int_{\Omega_P} \frac{\kappa}{\mu_f} \nabla e^n_{p_P,h} \cdot \nabla e^n_{p_P,h} \\
&\quad + \frac{1}{2} \partial_t^n \frac{1}{\lambda} \int_{\Omega_P} (\alpha \, e_{p_P,h} - e_{\varphi,h})^2 + \frac{1}{2} \Delta t \frac{1}{\lambda} \int_{\Omega_P} (\partial_t^n (\alpha \, e_{p_P,h} - e_{\varphi,h}))^2 = \mathcal{L}^n,
\end{aligned} \tag{5.7}
$$

where $\mathcal{L}^n$ is the collection of terms that appear on the right-hand sides in (5.6). Using the continuity of the bilinear forms (cf. Lemma 4.1) in combination with Young's inequality, we have

$$
\begin{aligned}
\mathcal{L}^n \leq \; & \epsilon \big(\|e^n_{\boldsymbol{u},h}\|^2_{\mathbf{H}^1(\Omega_F)} + \|e^n_{p_F,h}\|^2_{L^2(\Omega_F)} + \|e^n_{p_P,h}\|^2_{H^1(\Omega_P)} + \|e^n_{\varphi,h}\|^2_{L^2(\Omega_P)} \big) \\
& + C_\epsilon \big(\|e^n_{\boldsymbol{u},I}\|^2_{\mathbf{H}^1(\Omega_F)} + \|e^n_{p_F,I}\|^2_{L^2(\Omega_F)} + \|e^n_{p_P,I}\|^2_{H^1(\Omega_P)} + \|\partial_t^n e_{\boldsymbol{d},I}\|^2_{\mathbf{H}^1(\Omega_P)} + \|\partial_t^n e_{p_P,I}\|^2_{H^1(\Omega_P)} \\
& + \|\partial_t^n e_{\varphi,I}\|^2_{L^2(\Omega_P)} + \|r^n_{\boldsymbol{d}}\|^2_{\mathbf{L}^2(\Sigma)} + \|r^n_{p_P}\|^2_{L^2(\Omega_P)} + \|r^n_{\varphi}\|^2_{L^2(\Omega_P)} \big) + \mathcal{H}(\partial_t^n e_{\boldsymbol{d},h}),
\end{aligned} \tag{5.8}
$$

where $\mathcal{H}(\partial_t^n e_{\boldsymbol{d},h})$ is the collection of terms on the right-hand side of (5.6c) with $w_h = \partial_t^n e_{\boldsymbol{d},h}$. Multiplying (5.7) by Δt, summing for n from 1 to $k \in \{1, \ldots, N\}$, and using (5.8), we obtain

$$
\begin{aligned}
& \Delta t \sum_{n=1}^{k} \Big(\|e^n_{\boldsymbol{u},h}\|^2_{\mathbf{H}^1(\Omega_F)} + \sum_{j=1}^{d-1} \|(e^n_{\boldsymbol{u},h} - \partial_t^n e_{\boldsymbol{d},h}) \cdot \boldsymbol{t}^j\|^2_{L^2(\Sigma)} + \|e^n_{p_P,h}\|^2_{H^1(\Omega_P)} \Big) \\
& \quad + \|e^k_{\boldsymbol{d},h}\|^2_{\mathbf{H}^1(\Omega_P)} + \|e^k_{p_P,h}\|^2_{L^2(\Omega_P)} + \frac{1}{\lambda} \|\alpha e^k_{p_P,h} - e^k_{\varphi,h}\|^2_{L^2(\Omega_P)} \\
& \quad \leq C \Delta t \sum_{n=1}^{k} \Big(\epsilon \big(\|e^n_{\boldsymbol{u},h}\|^2_{\mathbf{H}^1(\Omega_F)} + \|e^n_{p_F,h}\|^2_{L^2(\Omega_F)} + \|e^n_{p_P,h}\|^2_{H^1(\Omega_P)} + \|e^n_{\varphi,h}\|^2_{L^2(\Omega_P)} \big) \\
& \qquad + C_\epsilon \big(\|e^n_{\boldsymbol{u},I}\|^2_{\mathbf{H}^1(\Omega_F)} + \|e^n_{p_F,I}\|^2_{L^2(\Omega_F)} + \|e^n_{p_P,I}\|^2_{H^1(\Omega_P)} + \|\partial_t^n e_{\boldsymbol{d},I}\|^2_{\mathbf{H}^1(\Omega_P)} + \|\partial_t^n e_{p_P,I}\|^2_{H^1(\Omega_P)} \\
& \qquad + \|\partial_t^n e_{\varphi,I}\|^2_{L^2(\Omega_P)} + \|r^n_{\boldsymbol{d}}\|^2_{\mathbf{L}^2(\Sigma)} + \|r^n_{p_P}\|^2_{L^2(\Omega_P)} + \|r^n_{\varphi}\|^2_{L^2(\Omega_P)} \big) + \mathcal{H}(\partial_t^n e_{\boldsymbol{d},h}) \Big) \\
& \qquad + C \big(\|e^0_{\boldsymbol{d},h}\|^2_{\mathbf{H}^1(\Omega_P)} + \|e^0_{p_P,h}\|^2_{L^2(\Omega_P)} + \frac{1}{\lambda} \|\alpha e^0_{p_P,h} - e^0_{\varphi,h}\|^2_{L^2(\Omega_P)} \big),
\end{aligned} \tag{5.9}
$$

where we also used Korn's inequality (4.5), the Poincaré inequality (4.4), and the permeability bound (4.7). Next, for each term in $\mathcal{H}(\partial_t^n e_{\boldsymbol{d},h})$ we use summation by parts:

$$
\Delta t \sum_{n=1}^{k} \phi^n \partial_t^n e_{\boldsymbol{d},h} = \phi^k e^k_{\boldsymbol{d},h} - \phi^1 e^0_{\boldsymbol{d},h} - \Delta t \sum_{n=2}^{k} \partial_t^n \phi \, e^{n-1}_{\boldsymbol{d},h},
$$

where ϕ stands for any of the functions that appear in $\mathcal{H}(\partial_t^n e_{\boldsymbol{d},h})$. Then, for the first term in $\mathcal{H}(\partial_t^n e_{\boldsymbol{d},h})$ we write, using Young's inequality,

$$
\begin{aligned}
\Delta t \sum_{n=1}^{k} b_3^\Sigma(e^n_{\boldsymbol{u},I}, \partial_t^n e_{\boldsymbol{d},h}) &= b_3^\Sigma(e^k_{\boldsymbol{u},I}, e^k_{\boldsymbol{d},h}) - b_3^\Sigma(e^1_{\boldsymbol{u},I}, e^0_{\boldsymbol{d},h}) - \Delta t \sum_{n=2}^{k} b_3^\Sigma(\partial_t^n e_{\boldsymbol{u},I}, e^{n-1}_{\boldsymbol{d},h}) \\
&\leq \epsilon \|e^k_{\boldsymbol{d},h}\|^2_{\mathbf{H}^1(\Omega_P)} + C_\epsilon \|e^k_{\boldsymbol{u},I}\|^2_{\mathbf{H}^1(\Omega_F)} + C \big(\|e^0_{\boldsymbol{d},h}\|^2_{\mathbf{H}^1(\Omega_P)} + \|e^1_{\boldsymbol{u},I}\|^2_{\mathbf{H}^1(\Omega_F)} \big) \\
&\quad + C \Delta t \sum_{n=2}^{k} \big(\|e^{n-1}_{\boldsymbol{d},h}\|^2_{\mathbf{H}^1(\Omega_P)} + \|\partial_t^n e_{\boldsymbol{u},I}\|^2_{\mathbf{H}^1(\Omega_F)} \big).
\end{aligned} \tag{5.10}
$$

Now, combining (5.9)–(5.10), and using for the rest of the terms in $\mathcal{H}(\partial_t^n e_{\boldsymbol{d},h})$ bounds that are similar to (5.10), we arrive at

$$\begin{aligned}
&\Delta t\sum_{n=1}^{k}\Big(\|e^n_{\boldsymbol{u},h}\|^2_{\mathbf{H}^1(\Omega_F)}+\sum_{j=1}^{d-1}\|(e^n_{\boldsymbol{u},h}-\partial_t^n e_{\boldsymbol{d},h})\cdot\boldsymbol{t}^j\|^2_{L^2(\Sigma)}+\|e^n_{p_P,h}\|^2_{H^1(\Omega_P)}\Big)\\
&\quad+\|e^k_{\boldsymbol{d},h}\|^2_{\mathbf{H}^1(\Omega_P)}+\|e^k_{p_P,h}\|^2_{L^2(\Omega_P)}+\frac{1}{\lambda}\|\alpha e^k_{p_P,h}-e^k_{\varphi,h}\|^2_{L^2(\Omega_P)}\\
&\quad\le C\Delta t\sum_{n=1}^{k}\Big(\epsilon\big(\|e^n_{\boldsymbol{u},h}\|^2_{\mathbf{H}^1(\Omega_F)}+\|e^n_{p_F,h}\|^2_{L^2(\Omega_F)}+\|e^n_{p_P,h}\|^2_{H^1(\Omega_P)}+\|e^n_{\varphi,h}\|^2_{L^2(\Omega_P)}\big)\\
&\qquad+\|e^n_{\boldsymbol{u},I}\|^2_{\mathbf{H}^1(\Omega_F)}+\|e^n_{p_F,I}\|^2_{L^2(\Omega_F)}+\|e^n_{p_P,I}\|^2_{H^1(\Omega_P)}+\|r^n_{\boldsymbol{d}}\|^2_{\mathbf{L}^2(\Sigma)}+\|r^n_{p_P}\|^2_{L^2(\Omega_P)}+\|r^n_{\varphi}\|^2_{L^2(\Omega_P)}\\
&\qquad+\|\partial_t^n e_{\boldsymbol{d},I}\|^2_{\mathbf{H}^1(\Omega_P)}+\|\partial_t^n e_{p_P,I}\|^2_{H^1(\Omega_P)}+\|\partial_t^n e_{\varphi,I}\|^2_{L^2(\Omega_P)}+\|\partial_t^n e_{\boldsymbol{u},I}\|^2_{\mathbf{H}^1(\Omega_F)}\Big)\\
&\qquad+C\Big(\Delta t\sum_{n=2}^{k}\big(\|e^{n-1}_{\boldsymbol{d},h}\|^2_{\mathbf{H}^1(\Omega_P)}+\|\partial_t^n\partial_t^n e_{\boldsymbol{d},I}\|^2_{\mathbf{H}^1(\Omega_P)}+\|\partial_t^n r_{\boldsymbol{d}}\|^2_{\mathbf{L}^2(\Sigma)}\big)\\
&\qquad\quad+\|e^0_{\boldsymbol{d},h}\|^2_{\mathbf{H}^1(\Omega_P)}+\|e^0_{p_P,h}\|^2_{L^2(\Omega_P)}+\frac{1}{\lambda}\|\alpha e^0_{p_P,h}-e^0_{\varphi,h}\|^2_{L^2(\Omega_P)}+\|\partial_t^k e_{\boldsymbol{d},I}\|^2_{\mathbf{H}^1(\Omega_P)}+\|\partial_t^1 e_{\boldsymbol{d},I}\|^2_{\mathbf{H}^1(\Omega_P)}\\
&\qquad\quad+\|e^k_{\boldsymbol{u},I}\|^2_{\mathbf{H}^1(\Omega_F)}+\|e^k_{\boldsymbol{d},I}\|^2_{\mathbf{H}^1(\Omega_P)}+\|e^k_{p_P,I}\|^2_{H^1(\Omega_P)}+\|e^k_{\varphi,I}\|^2_{L^2(\Omega_P)}+\|r^k_{\boldsymbol{d}}\|^2_{\mathbf{L}^2(\Sigma)}\\
&\qquad\quad+\|e^1_{\boldsymbol{u},I}\|^2_{\mathbf{H}^1(\Omega_F)}+\|e^1_{\boldsymbol{d},I}\|^2_{\mathbf{H}^1(\Omega_P)}+\|e^1_{p_P,I}\|^2_{H^1(\Omega_P)}+\|e^1_{\varphi,I}\|^2_{L^2(\Omega_P)}+\|r^1_{\boldsymbol{d}}\|^2_{\mathbf{L}^2(\Sigma)}\Big).
\end{aligned}\tag{5.11}$$

We continue with bounding $\|e^n_{p_F,h}\|^2_{L^2(\Omega_F)}$ and $\|e^n_{\varphi,h}\|^2_{L^2(\Omega_P)}$, which appear on the right-hand side above. The inf-sup condition (4.1a) and (5.6a) imply

$$\begin{aligned}
\Delta t\sum_{n=1}^{k}\|e^n_{p_F,h}\|^2_{L^2(\Omega_F)}&\le C\Delta t\sum_{n=1}^{k}\Big(\|e^n_{\boldsymbol{u},h}\|^2_{\mathbf{H}^1(\Omega_F)}+\sum_{j=1}^{d-1}\|(e^n_{\boldsymbol{u},h}-\partial_t^n e_{\boldsymbol{d},h})\cdot\boldsymbol{t}^j\|^2_{L^2(\Sigma)}+\|e^n_{p_P,h}\|^2_{H^1(\Omega_P)}\\
&\quad+\|e^n_{\boldsymbol{u},I}\|^2_{\mathbf{H}^1(\Omega_F)}+\|e^n_{p_F,I}\|^2_{L^2(\Omega_F)}+\|e^n_{p_P,I}\|^2_{H^1(\Omega_P)}+\|\partial_t^n e_{\boldsymbol{d},I}\|^2_{\mathbf{H}^1(\Omega_P)}+\|r^n_{\boldsymbol{d}}\|^2_{\mathbf{L}^2(\Sigma)}\Big).
\end{aligned}$$

On the other hand, the inf-sup condition (4.1b) and (5.6c) allow us to get

$$\begin{aligned}
\Delta t\sum_{n=1}^{k}\|e^n_{\varphi,h}\|^2_{L^2(\Omega_P)}&\le C\Delta t\sum_{n=1}^{k}\Big(\|e^n_{p_P,h}\|^2_{H^1(\Omega_P)}+\sum_{j=1}^{d-1}\|(e^n_{\boldsymbol{u},h}-\partial_t^n e_{\boldsymbol{d},h})\cdot\boldsymbol{t}^j\|^2_{L^2(\Sigma)}+\|e^n_{\boldsymbol{d},h}\|^2_{\mathbf{H}^1(\Omega_P)}\\
&\quad+\|e^n_{\boldsymbol{u},I}\|^2_{\mathbf{H}^1(\Omega_F)}+\|e^n_{p_P,I}\|^2_{H^1(\Omega_P)}+\|e^n_{\boldsymbol{d},I}\|^2_{\mathbf{H}^1(\Omega_P)}+\|\partial_t^n e_{\boldsymbol{d},I}\|^2_{\mathbf{H}^1(\Omega_P)}+\|e^n_{\varphi,I}\|^2_{L^2(\Sigma)}+\|r^n_{\boldsymbol{d}}\|^2_{\mathbf{L}^2(\Sigma)}\Big).
\end{aligned}\tag{5.12}$$

Before combining (5.11)–(5.12), we note that the terms involving ∂_t^n on the right-hand sides require special treatment. In particular, it holds for $\phi(t)$ that

$$(\partial_t^n\phi)^2=\frac{1}{\Delta t^2}\Big(\int_{t_{n-1}}^{t_n}\partial_t\phi\Big)^2\le\frac{1}{\Delta t}\int_{t_{n-1}}^{t_n}(\partial_t\phi)^2,$$

implying, for $\phi:[0,T]\to V$, where V is a Banach space with norm $\|\cdot\|_V$, that

$$\Delta t\sum_{n=1}^{k}\|\partial_t^n\phi\|^2_V\le\int_0^{t_k}\|\partial_t\phi\|^2_V.$$

We then have

$$\begin{aligned}&\Delta t\sum_{n=1}^{k}\left(\|\partial_t^n e_{\boldsymbol{d},I}\|^2_{\mathbf{H}^1(\Omega_P)}+\|\partial_t^n e_{p_P,I}\|^2_{H^1(\Omega_P)}+\|\partial_t^n e_{\varphi,I}\|^2_{L^2(\Omega_P)}+\|\partial_t^n e_{\boldsymbol{u},I}\|^2_{\mathbf{H}^1(\Omega_F)}\right)\\&\quad\le C\int_0^{t_k}\left(\|\partial_t e_{\boldsymbol{d},I}\|^2_{\mathbf{H}^1(\Omega_P)}+\|\partial_t e_{p_P,I}\|^2_{H^1(\Omega_P)}+\|\partial_t e_{\varphi,I}\|^2_{L^2(\Omega_P)}+\|\partial_t e_{\boldsymbol{u},I}\|^2_{\mathbf{H}^1(\Omega_F)}\right).\end{aligned}\tag{5.13}$$

To bound the term $\|\partial_t^n\partial_t^n e_{\boldsymbol{d},I}\|^2_{\mathbf{H}^1(\Omega_P)}$ in (5.11), for any $\phi(t)$ we have, using the integral mean value theorem and the mean value theorem,

$$(\partial_t^n\partial_t^n\phi)^2=\frac{1}{\Delta t^4}\Big(\int_{t_{n-1}}^{t^n}\partial_t\phi-\int_{t_{n-2}}^{t^{n-1}}\partial_t\phi\Big)^2=\frac{1}{\Delta t^2}\big(\partial_t\phi(\xi^n)-\partial_t\phi(\xi^{n-1})\big)^2=\partial_{tt}\phi(\xi),\quad \xi\in[t_{n-2},t_n].$$

Therefore it holds that

$$\Delta t\sum_{n=2}^{k}\|\partial_t^n\partial_t^n e_{\boldsymbol{d},I}\|^2_{\mathbf{H}^1(\Omega_P)}\le C\operatorname*{ess\,sup}_{t\in(0,t_k)}\|\partial_{tt}e_{\boldsymbol{d},I}\|^2_{\mathbf{H}^1(\Omega_P)}.$$

Next, we need to bound the time discretisation error. Taylor's expansion gives

$$r_\phi^n=\frac{1}{\Delta t}\int_{t_n}^{t_{n-1}}\partial_{tt}\phi(t)(t_{n-1}-t)\,\mathrm{d}t,$$

thus, for $\phi:[0,T]\to V$,

$$\|r_\phi^n\|_V\le C\Delta t\operatorname*{ess\,sup}_{t\in(t_{n-1},t_n)}\|\partial_{tt}\phi\|_V\quad\text{and}\quad\Delta t\sum_{n=1}^{k}\|r_\phi^n\|_V^2\le C\Delta t^2\int_0^{t_k}\|\partial_{tt}\phi\|_V^2.$$

Similarly,

$$\Delta t\sum_{n=1}^{k}\|\partial_t^n r_\phi\|_V^2\le C\Delta t^2\int_0^{t_k}\|\partial_{ttt}\phi\|_V^2.$$

Finally, we need a bound on the initial discretisation error. Recalling the construction of the discrete initial data in the proof of Theorem 4.1 and the definition of the continuous initial data in the proof of Theorem 4.2, we note that $(\boldsymbol{u}_h^0,p_{F,h}^0)$ is the Stokes elliptic projection of $(\boldsymbol{u}(0),p_{F,h}(0))$ based on (4.2a)–(4.2b) at $t=0$ with $\partial_t\boldsymbol{d}_h=0$ and the term $b_2^\Sigma(p_{P,0}-p_{P,h,0},\boldsymbol{v}_h)$ on the right-hand side. In addition, $(\boldsymbol{d}_h^0,\varphi_h^0)$ is the elliptic projection of $(\boldsymbol{d}(0),\varphi(0))$ based on the stable problem (4.2c)–(4.2e) at $t=0$ with $\partial_t\boldsymbol{d}_h=0$ and the terms $b_3^\Sigma(\boldsymbol{u}(0)-\boldsymbol{u}_h^0,\boldsymbol{w}_h)$, $b_4^\Sigma(\boldsymbol{w}_h,p_{P,0}-p_{P,h,0})$, and $b_2^P(\psi_h,p_{P,0}-p_{P,h,0})$ on the right-hand side. Classical finite element analysis for these two problems implies that

$$\begin{aligned}&\|e^0_{\boldsymbol{u},h}\|_{\mathbf{H}^1(\Omega_F)}+\|e^0_{p_F,h}\|_{L^2(\Omega_F)}+\|e^0_{\boldsymbol{d},h}\|_{\mathbf{H}^1(\Omega_P)}+\|e^0_{p_P,h}\|_{L^2(\Omega_P)}+\|e^0_{\varphi,h}\|_{L^2(\Omega_P)}\\&\quad\le C\big(\|e^0_{\boldsymbol{u},I}\|_{\mathbf{H}^1(\Omega_F)}+\|e^0_{p_F,I}\|_{L^2(\Omega_F)}+\|e^0_{\boldsymbol{d},I}\|_{\mathbf{H}^1(\Omega_P)}+\|e^0_{p_P,I}\|_{L^2(\Omega_P)}+\|e^0_{\varphi,I}\|_{L^2(\Omega_P)}\big).\end{aligned}\tag{5.14}$$

The assertion of the theorem follows from combining (5.11)–(5.14), using the discrete Gronwall inequality [47, Lemma 1.4.2] for the term $\Delta t\sum_{n=2}^{k}\|e^{n-1}_{\boldsymbol{d},h}\|^2_{\mathbf{H}^1(\Omega_P)}$, and applying the triangle inequality and the approximation properties (5.4a)–(5.4e). □

DoF	h	$\mathtt{e}_{\boldsymbol{u}}$	rate	$\mathtt{e}_{p_F}$	rate	$\mathtt{e}_{\boldsymbol{d}}$	rate	$\mathtt{e}_{p_P}$	rate	$\mathtt{e}_{\varphi}$	rate
144	1.414	4.70604	–	0.82152	–	21.4632	–	2.80468	–	19.3402	–
456	0.7071	1.66701	1.497	0.29604	1.472	9.75813	1.137	0.84917	1.721	8.20939	1.236
1608	0.3536	0.40411	2.044	0.06081	2.260	2.78206	1.811	0.24942	1.769	1.21860	2.422
6024	0.1768	0.09746	2.051	0.01376	2.138	0.72730	1.936	0.06567	1.943	0.25337	2.240
23304	0.0884	0.02405	2.014	0.00328	2.052	0.18545	1.984	0.01661	1.985	0.05166	2.231
91656	0.0442	0.00597	2.005	0.00081	2.018	0.04683	1.991	0.00410	1.991	0.00472	2.098
363528	0.0221	0.00151	2.001	0.00022	2.008	0.01172	1.998	0.00100	1.995	0.00061	2.015

Table 6.1: Example 1. Experimental errors associated with the spatial discretisation and convergence rates for the approximate solutions $\boldsymbol{u}_h$, $p_{F,h}$, $\boldsymbol{d}_h$, $p_{P,h}$, and φ_h using $\mathbb{P}_2^2 - \mathbb{P}_1 - \mathbb{P}_2^2 - \mathbb{P}_2 - \mathbb{P}_1$ elements and computed at the last time step.

6. Representative computational results

All routines have been implemented using the open source finite element library `FEniCS` [4], as well as the specialised module `multiphenics` [10] for handling subdomain- and boundary- restricted terms that we require to impose transmission conditions across interfaces. The solvers are monolithic and the solution of all linear systems is performed with the distributed direct solver MUMPS. We present four examples: convergence tests (example 1), channel flow behaviour (example 2), a simulation of subsurface flow with heterogeneous random permeability (example 3), and the solution of an axisymmetric problem using parameters relevant to eye poromechanics (example 4). For examples 1,2 and 4 we use Taylor-Hood elements for the pairs velocity-pressure and displacement - total pressure, plus continuous and piecewise quadratic elements for Biot fluid pressure. For example 3, the inf-sup stable pair used is the MINI element, and the Biot fluid pressure is approximated with continuous and piecewise linear elements.

6.1. Convergence tests against manufactured solutions

The accuracy of the spatio-temporal discretisation is verified using the following closed-form solutions defined on the domains $\Omega_F = (-1,1)\times(0,2)$, $\Omega_P = (-1,1)\times(-2,0)$, separated by the interface $\Sigma = (-1,1)\times\{0\}$

$$\begin{aligned} \boldsymbol{u} &= \sin(t)\begin{pmatrix} -\cos(\pi x)\sin(\pi y) \\ \sin(\pi x)\cos(\pi y)\end{pmatrix}, \quad p_F = \sin(t)\cos(\pi x)\cos(\pi y), \\ \boldsymbol{d} &= \cos(t)\,\mathrm{curl}(\sin(\pi x y)), \quad p_P = \cos(t)\sin(\pi x)\sin(\pi y), \quad \varphi = \alpha p_P - \lambda\,\mathrm{div}\,\boldsymbol{d}. \end{aligned} \tag{6.1}$$

We consider Γ_P^p to be the bottom horizontal segment, $\Gamma_P^{\boldsymbol{d}}$ to be the lower vertical walls, $\Gamma_F^{\boldsymbol{u}}$ to be the top horizontal segment, and $\Gamma_F^{\boldsymbol{\sigma}}$ to be the upper vertical walls. the synthetic model parameters are taken as

$$\lambda = 1000, \quad \mu_s = 1, \quad \mu_f = 0.1, \quad \alpha = \gamma = 1, \quad c_0 = 0.01, \quad \kappa = 0.001, \quad \rho_s = 1.2, \quad \rho_f = 1,$$

all regarded adimensional and do not have physical relevance in this case, as we will be simply testing the convergence of the finite element approximations. The manufactured solutions (6.1) are used to prescribe initial conditions, essential non-homogeneous velocity and displacement boundary conditions,

Δt	$\hat{\mathrm{e}}_{\boldsymbol{u}}$	rate	$\hat{\mathrm{e}}_{p_F}$	rate	$\hat{\mathrm{e}}_{\boldsymbol{d}}$	rate	$\hat{\mathrm{e}}_{p_P}$	rate	$\hat{\mathrm{e}}_{\varphi}$	rate
0.5	10.549	–	2.5844	–	43.764	–	8.6738	–	38.734	–
0.25	5.1408	0.984	1.2710	1.163	21.840	1.211	4.3673	1.125	19.371	1.055
0.125	2.2689	1.205	0.6485	1.182	10.661	1.204	2.1690	1.032	9.6901	0.962
0.0625	1.1365	1.107	0.3216	1.095	5.4517	1.121	1.0795	1.025	4.8614	0.981
0.03125	0.6813	1.004	0.1615	1.071	2.7326	1.043	0.5527	0.987	2.4396	0.992

Table 6.2: Example 1. Experimental cumulative errors associated with the temporal discretisation and convergence rates for the approximate solutions $\boldsymbol{u}_h$, $p_{F,h}$, $\boldsymbol{d}_h$, $p_{P,h}$, and φ_h using a backward Euler scheme.

as well as natural non-homogeneous flux conditions for fluid pressure. These functions do not necessarily fulfil the interface conditions, so additional terms are required giving modified relations on Σ:

$$\boldsymbol{u}\cdot\boldsymbol{n}-(\partial_t\boldsymbol{d}-\frac{\kappa}{\mu_f}\nabla p_P)\cdot\boldsymbol{n}=m^1_{\Sigma,\mathrm{ex}},\qquad (2\mu_f\boldsymbol{\epsilon}(\boldsymbol{u})-p_F\mathbf{I})\boldsymbol{n}-(2\mu_s\boldsymbol{\epsilon}(\boldsymbol{d})-\varphi\mathbf{I})\boldsymbol{n}=\boldsymbol{m}^2_{\Sigma,\mathrm{ex}},$$
$$\boldsymbol{n}\cdot(2\mu_f\boldsymbol{\epsilon}(\boldsymbol{u})-p_F\mathbf{I})\boldsymbol{n}+p_P=m^3_{\Sigma,\mathrm{ex}},\qquad \boldsymbol{n}\cdot(2\mu_f\boldsymbol{\epsilon}(\boldsymbol{u})-p_F\mathbf{I})\boldsymbol{t}+\frac{\gamma\mu_f}{\sqrt{\kappa}}(\boldsymbol{u}-\partial_t\boldsymbol{d})\cdot\boldsymbol{t}=m^4_{\Sigma,\mathrm{ex}},$$

and the additional scalar and vector terms $m^i_{\Sigma,\mathrm{ex}}$ (computed with the exact solutions (6.1)) entail the following changes in the linear functionals

$$F^F(\boldsymbol{v})=\rho_f\int_{\Omega_F}\boldsymbol{g}\cdot\boldsymbol{v}+\langle m^3_{\Sigma,\mathrm{ex}},\boldsymbol{v}\cdot\boldsymbol{n}\rangle_\Sigma+\langle m^4_{\Sigma,\mathrm{ex}},\boldsymbol{v}\cdot\boldsymbol{t}\rangle_\Sigma,$$
$$F^P(\boldsymbol{w})=\rho_s\int_{\Omega_P}\boldsymbol{f}\cdot\boldsymbol{w}+\int_{\Omega_P}\boldsymbol{m}^2_{\Sigma,\mathrm{ex}}\cdot\boldsymbol{w}+\langle m^3_{\Sigma,\mathrm{ex}},\boldsymbol{w}\cdot\boldsymbol{n}\rangle_\Sigma+\langle m^4_{\Sigma,\mathrm{ex}},\boldsymbol{w}\cdot\boldsymbol{t}\rangle_\Sigma,$$
$$G(q_P)=\int_{\Omega_P}\rho_f\boldsymbol{g}\cdot\nabla q_P-\langle\rho_f\boldsymbol{g}\cdot\boldsymbol{n},q_P\rangle_\Sigma-\langle m^1_{\Sigma,\mathrm{ex}},q_P\rangle_\Sigma.$$

We generate successively refined simplicial grids and use a sufficiently small (non dimensional) time step $\Delta t=0.01$ and simulate a relatively short time horizon $t_{\mathrm{final}}=3\Delta t$, to guarantee that the error produced by the time discretisation does not dominate. Errors between the approximate and exact solutions are tabulated against the number of degrees of freedom in Table 6.1. This error history confirms the optimal convergence of the finite element scheme (in this case, second-order) for all variables in their respective norms, where a slightly better rate is seen for the total pressure. In the table caption, $\mathbb{P}_k$ denotes the space of piecewise polynomial functions being of total degree up to k.

For this example we have reincorporated the acceleration and the nonlinear convective term, and the Newton-Raphson algorithm takes, in average, three iterations to reach the prescribed tolerance of 10^{-8} on the residuals.

The convergence in time achieved by the backward Euler method is verified by partitioning the time interval $(0,1)$ into successively refined uniform discretisations and computing accumulated errors

$$\hat{\mathrm{e}}_s=\left(\sum_{n=1}^{N}\Delta t\|s(t_{n+1})-s_h^{n+1}\|^2_\star\right)^{1/2},$$

where $\|\cdot\|_\star$ denotes the appropriate space norm for the generic vector or scalar field s. For this test we use a fixed mesh involving 10K DoFs. The results are shown in Table 6.2, confirming the optimal first-order convergence.

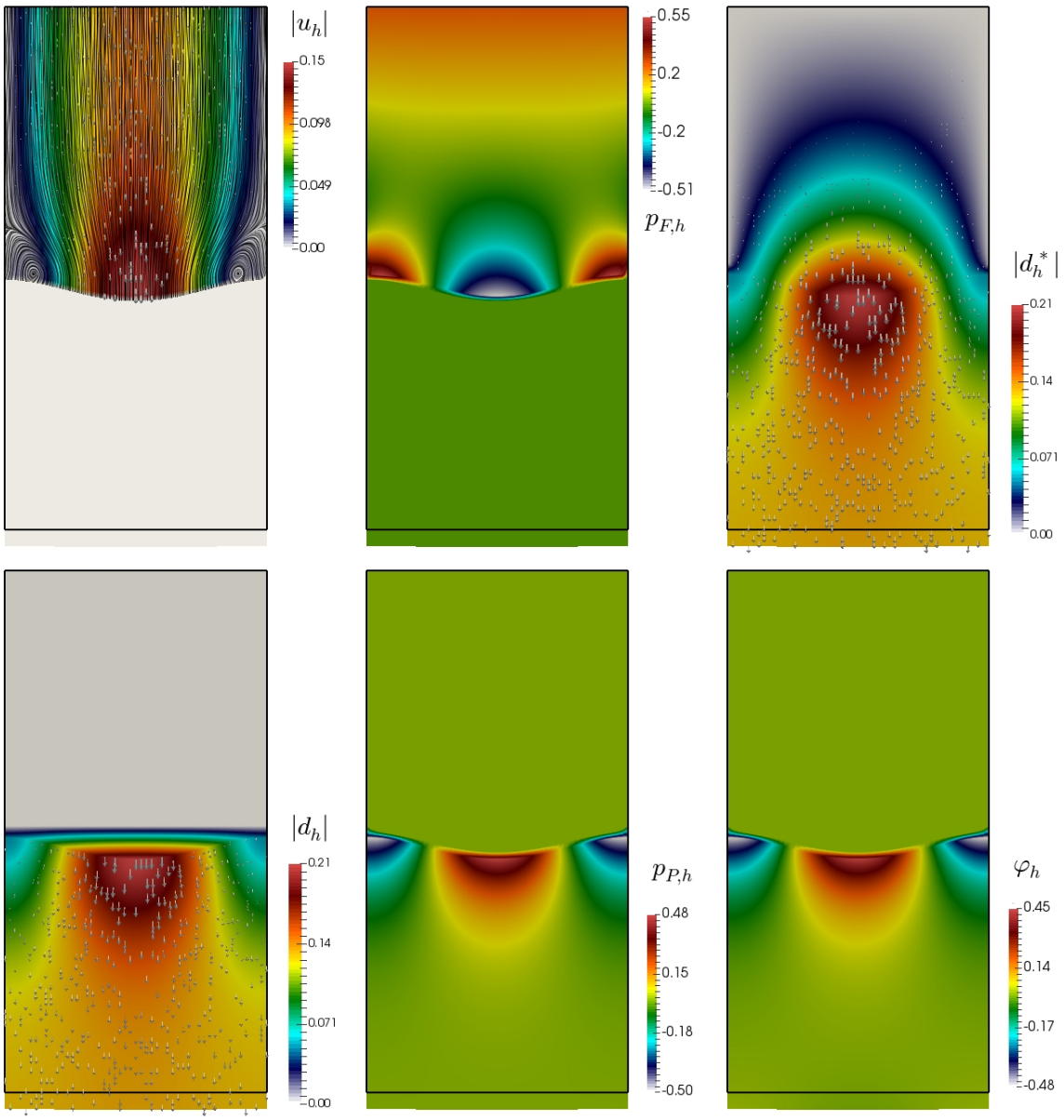

Figure 6.1: Example 2. Infiltration into a deformable porous medium. Velocity in the fluid domain, fluid pressure, extended displacement of fluid and solid domains, solid displacement, fluid pressure in the poroelastic domain, and total pressure. All snapshots are taken at time $t = 2$, and the black outer line indicates the location of the undeformed domain.

6.2. Channel filtration and stress build-up on interface deformation

Although the model stated in Section 2 holds in the limit of small strains, it is possible to have large displacements, likely located near the interface (and without violating the model assumptions). In this scenario, the discretisation might no longer be suitable. A simple remedy consists in smoothly moving the fluid domain and the fluid mesh to avoid distortions generated near the interface. We use a standard harmonic extension (see e.g. [16]) that is solved at each time step, just after (5.2): Find $\boldsymbol{d}_h^* = \boldsymbol{d}_h + \widehat{\boldsymbol{d}}_h$ such that

$$-D\Delta\widehat{\boldsymbol{d}}_h = \boldsymbol{0} \quad \text{in } \Omega_F, \qquad \widehat{\boldsymbol{d}}_h = \boldsymbol{d}_h \text{ on } \Sigma, \qquad \text{and} \qquad \widehat{\boldsymbol{d}}_h = \boldsymbol{0} \text{ on } \partial\Omega_F. \tag{6.2}$$

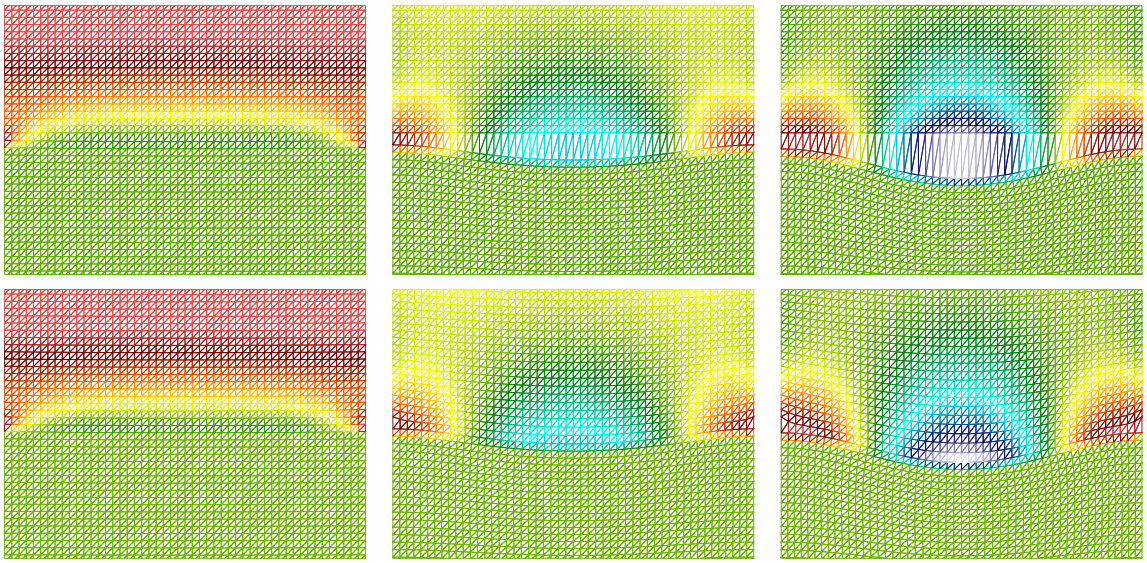

Figure 6.2: Example 2. Zoom of the meshes on the interface at times $t = 0$, $t = 1$ and $t = 2$. Effect of using or not the harmonic extension to move the fluid domain (bottom and top, respectively).

And then we perform an L^2-projection of both $\boldsymbol{d}_h$ and $\widehat{\boldsymbol{d}}_h$ into $\mathbf{W}_h + \mathbf{V}_h$ and add them to obtain the global displacement $\boldsymbol{d}_h^*$.

We illustrate the effect of using (6.2) by looking at the behaviour of normal filtration into a 2D deformable porous medium. The same domains as in the accuracy tests are employed here (that is, the single phase fluid domain located on top of the poroelastic domain), however the boundary treatment is as follows, assuming that the flow is driven by pressure differences only. On the top segment we impose the fluid pressure $p_F^{\text{in}} = p_0 \sin^2(\pi t)$ with $p_0 = 2$, and on the outlet (the bottom segment) the fluid pressure $p_P^{\text{out}} = 0$. On the vertical walls of Ω_F we set $\boldsymbol{u} = \mathbf{0}$ while on the vertical walls of Ω_P we set the slip condition $\boldsymbol{d} \cdot \boldsymbol{n} = 0$ (and the porous structure is free to deform on the outlet boundary, i.e., zero traction imposed). The permeability is $\kappa = 0.02$ and the remaining parameters are

$$\lambda = 10, \quad \mu_s = 5, \quad \rho_s = 1.1, \quad \rho_f = 1, \quad \alpha = 0.6, \quad \gamma = 0.1, \quad C_0 = 0.01,$$

and we assume that there are no body forces nor gravity acting on the system. In contrast with the convergence tests, for this example we use piecewise linear and continuous finite elements for the approximation of p_P.

The numerical results are presented in Figure 6.1. The effect of the interface can be clearly seen in the top left panel where recirculation vortices replace the parabolic profile at the inlet; also, in the poroelastic domain, we see that, close to the interface, the solid displacement and the fluid pressure are heterogeneous in the horizontal direction, before recovering the expected constant value (constant in the horizontal direction) expected in the far field. We also plot the evolution of the mesh deformation near the interface. From Figure 6.2 one can see that for large enough interfacial displacements, the elements close to it exhibit a large distortion.

6.3. Simulation of subsurface fracture flow

Next we include a test case that illustrates the applicability of the formulation in hydraulic fracturing. The problem setup follows [6, Section 5.2.2] (except that we do not model tracer transport),

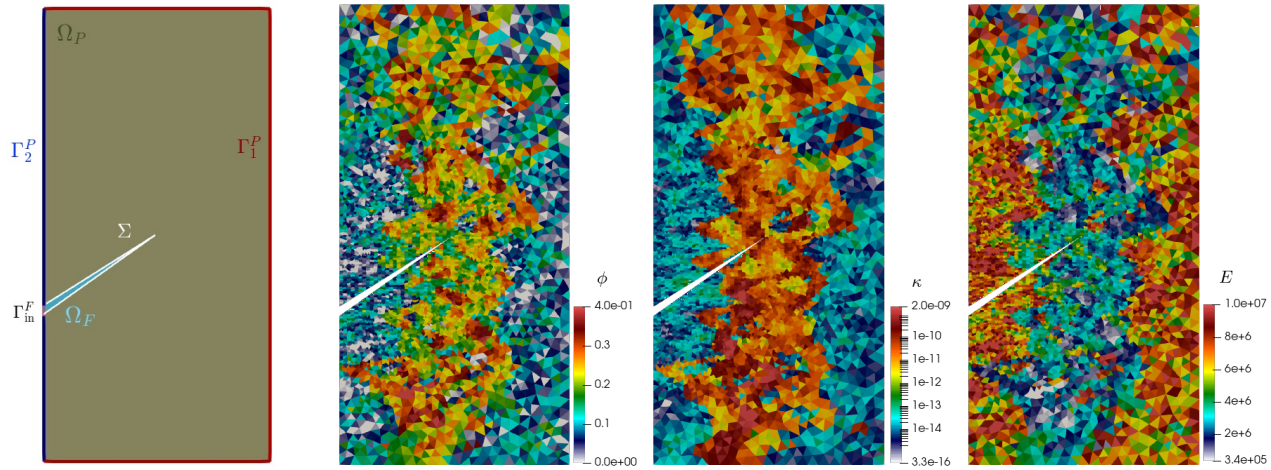

Figure 6.3: Example 3. Schematic representation of sub-domains, location of the free-porous interface, and configuration of sub-boundaries (left panel); and material properties (porosity $\phi(\boldsymbol{x})$, permeability $\kappa(\boldsymbol{x})$, and Young modulus $E(\boldsymbol{x})$) from layer 80 of the SPE10 benchmark dataset for reservoir simulations, herein projected onto a coarse mesh for the poroelastic sub-domain.

considering a rectangular domain $\Omega = (0, 3.048)\,[\text{m}] \times (0, 6.096)\,[\text{m}]$ including a relatively large fracture regarded as a macro void, or open channel Ω_F filled with an incompressible fluid (see Figure 6.3, left), and the Biot domain is $\Omega_P = \Omega \setminus \Omega_F$. The heterogeneous (but isotropic in the xy-plane) permeability $\kappa(\boldsymbol{x})$ is the non-smooth pattern taken from the Cartesian SPE10 benchmark data / model 2 (see, e.g., [1, 21]), which we rescale as in [7] and project onto a piecewise constant field defined on an unstructured triangular mesh for the poroelastic geometry. There are 85 distinct layers within two general categories. We choose layer 80 from the dataset, which corresponds to the Upper Ness region exhibiting a fluvial fan pattern (flux channels of higher permeability and porosity). The Lamé parameters (in [KPa]) are highly heterogeneous and determined from the Poisson ratio $\nu = 0.2$ and the Young modulus $E(\boldsymbol{x}) = 10^7(1 - 2\phi(\boldsymbol{x}))^{2.1}$, where $\phi(\boldsymbol{x})$ is the porosity field also taken from layer 80 of the benchmark dataset (see Figure 6.3, right). It is plotted in logarithmic scale and the contrast is of about 10^8. No gravity and no external loads are considered, and the remaining parameters are $\alpha = \gamma = 1$, $c_0 = 6.89 \cdot 10^{-2}\,[\text{KPa}^{-1}]$, $\mu_f = 10^{-6}\,[\text{KPa} \cdot \text{s}]$.

Similarly as in [7], we set the flow initially at rest $\boldsymbol{d}(0) = \boldsymbol{0}$ and the initial Biot pressures are $p_P(0) = \varphi(0) = 1000\,[\text{KPa}]$ (since $\alpha = 1$). On the inlet boundary $\Gamma_{\rm in}^F$ (the vertical segment on the Stokes boundary) we impose the inflow velocity $\boldsymbol{u} = (10, 0)^{\mathtt{t}}\,[\text{m/s}]$, on the bottom, right and top sub-boundaries Γ_1^P of the Biot domain we prescribe sliding conditions $\boldsymbol{d} \cdot \boldsymbol{n} = 0\,[\text{m}]$ together with a compatible normal-tangential stress condition and a fixed Biot pressure $p_P = 1000\,[\text{KPa}]$, and on the right sub-boundaries Γ_2^P of the Biot domain we set stress-free conditions. The time discretisation uses the fixed time step $\Delta t = 60\,[\text{s}]$ and we run the simulation of injection over a period of $T = 10\,[\text{hours}]$. The unstructured triangular mesh has 1629 elements for the Stokes sub-mesh and 18897 elements for the Biot domain. For this test we have used the MINI element, consisting of continuous and piecewise linear elements with bubble enrichment for velocity and displacement, and continuous and piecewise linear elements for all remaining fields. The injected fluid imposes an increase of pressure on the interface and from there the expected channel-like progressive filtration from the Stokes to the Biot domain is clearly observed in the Biot pressure plot in the left panel of Figure 6.4, showing higher fluxes near the tip of the fracture. The remaining panels show, at the final time, snapshots of Stokes velocity, Biot displacement, and post-processed Biot filtration velocity. The deformation of the poroelastic structure

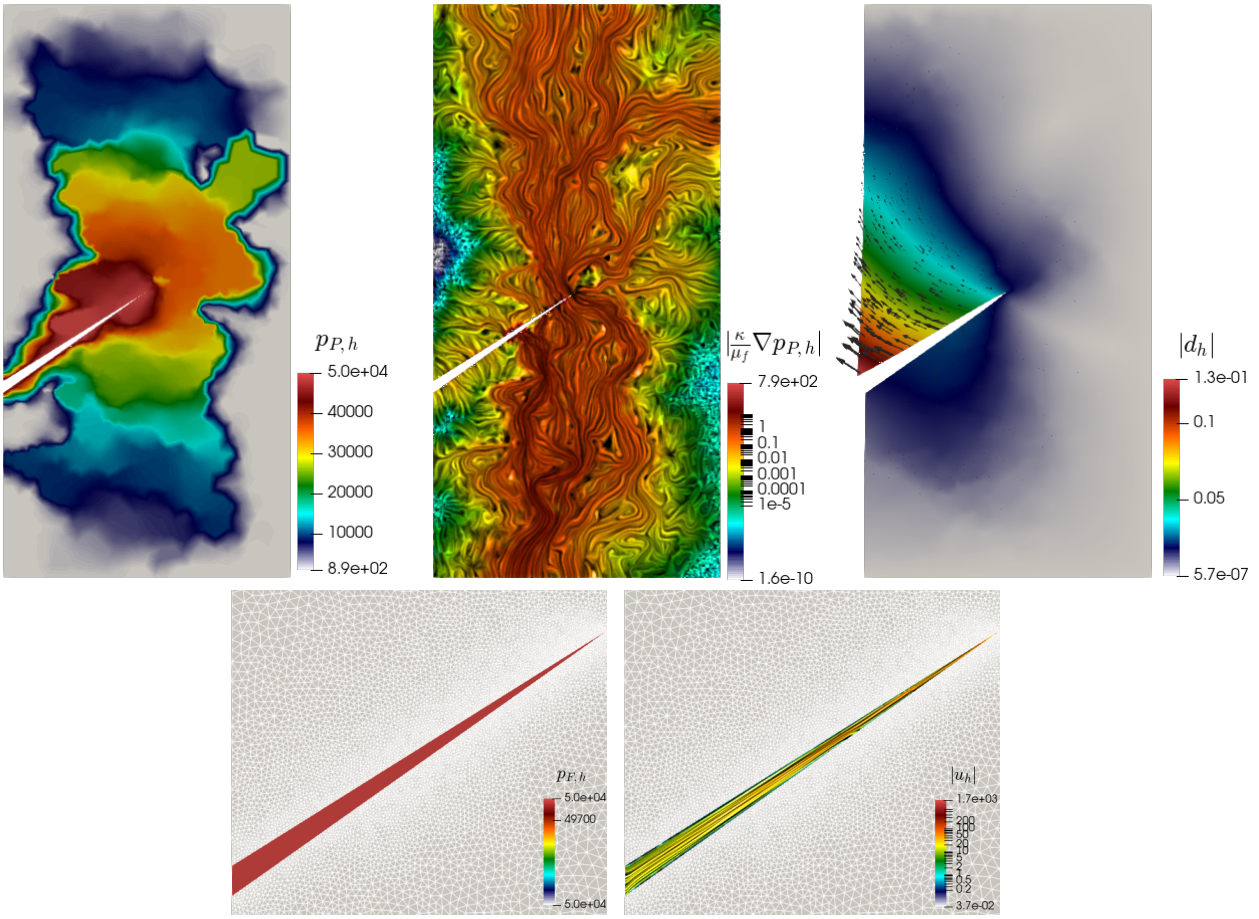

Figure 6.4: Example 3. Snapshots of the approximate solutions (Biot fluid pressure, post-processed Biot fluid velocity and line integral convolution, Biot displacement magnitude and displacement arrows on the deformed domain, Stokes fluid pressure, and Stokes velocity magnitude with line integral convolution) for fluid injection into a fracture porous medium using the SPE10-based benchmark test. Results were obtained after $t = 10\,[\text{hours}]$.

closer to the fracture is relatively small, which is why we do not consider in this test the harmonic extension of the fluid domain addressed in the previous example.

6.4. Application to interfacial flow in the eye

To finalise this section we include a problem pertaining to the application of the interaction between aqueous humour in the anterior chamber and the trabecular meshwork. Therein, one of the main driving questions is whether one can observe deformation of the porous skeleton (and in particular of the interface) that could drive a rise in intra-ocular pressure. For this test we use the axisymmetric formulation (3.3), we include the convective term in (2.1a) and we discard gravity. A large amount of data is available to specialise the geometry and the mechanical properties (both fluidic and elastic) of the eye to different animal species [18, 35, 29, 42]. In our case (and consistent with a uniform temperature of 37° and a characteristic length of $6.8 \cdot 10^{-3}\,[\text{m}]$) we impose

$$\rho_f = 998.7\,[\text{Kg}\cdot\text{m}^{-3}], \quad \mu_f = 7.5\cdot 10^{-4}\,[\text{Pa}\cdot\text{s}], \quad p_0 = 0\,[\text{Pa}], \quad E = 2700\,[\text{Pa}], \quad \nu = 0.47,$$
$$\lambda = 14388\,[\text{Pa}], \quad \mu_s = 918.36\,[\text{Pa}], \quad \alpha = 1, \quad \rho_s = 1102\,[\text{Kg}\cdot\text{m}^{-3}], \quad C_0 = 0, \quad \gamma = 0.1.$$

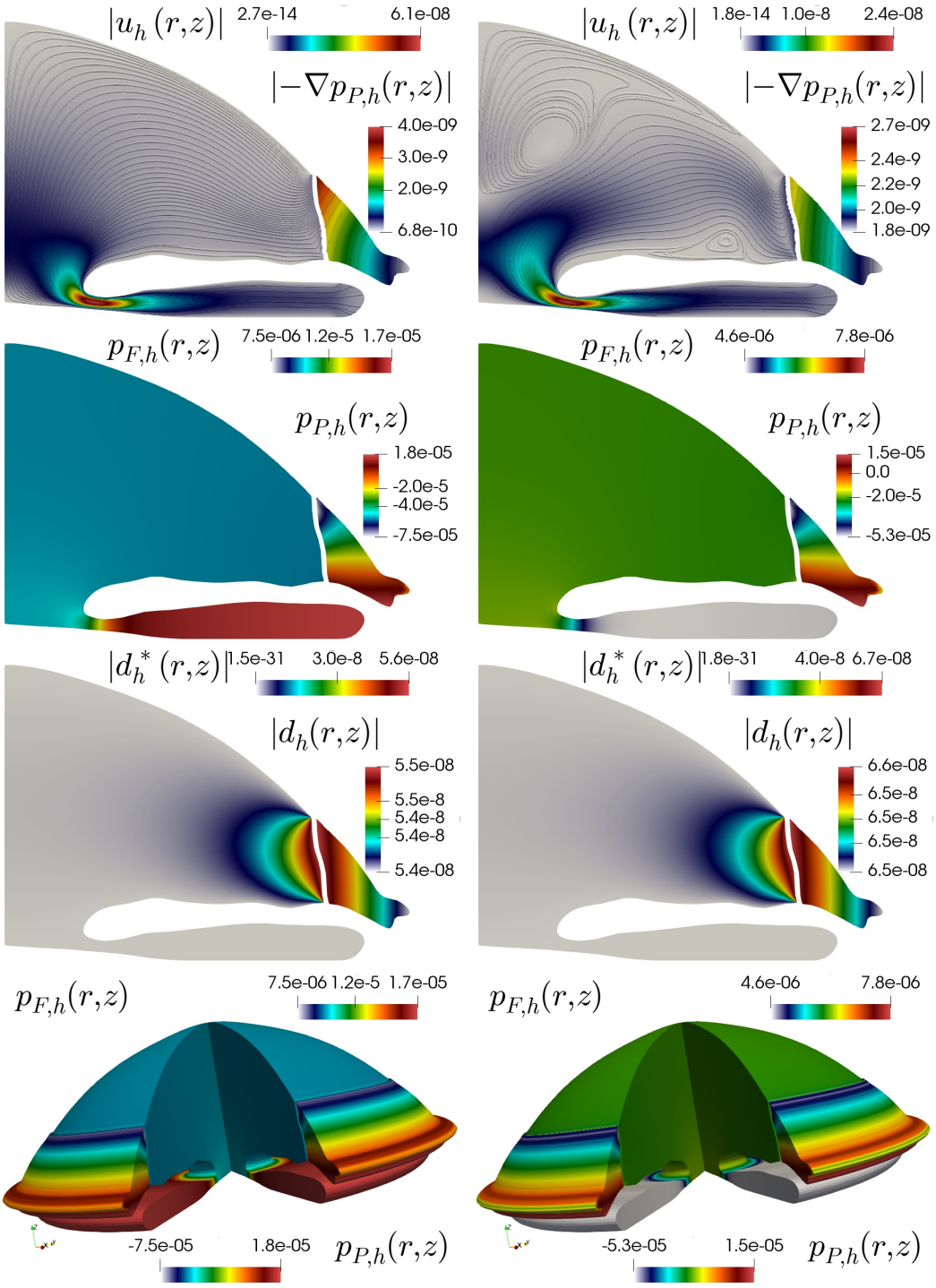

Figure 6.5: Example 4. Axisymmetric interfacial flow in the eye for a linearly varying permeability profile. Velocity magnitude and streamlines (top), fluid pressure (second row), displacement magnitude (third row), porous total pressure, and fluid pressures on both domains extruded to the 3D case (bottom centre and bottom right). All solutions are shown at times $t = 4.2$ [s] (left) and $t = 5$ [s] (right column).

As discussed in [25], an increase in the Beavers-Joseph-Saffmann friction parameter γ leads to higher

pressure differences between the trabecular meshwork and the anterior chamber. Note that even if the choice of $\alpha = 1$, $C_0 = 0$ indicates that both constituents (fluid and solid) are assumed intrinsically incompressible, a Poisson ratio smaller than 0.5 implies compressibility of the poroelastic medium (due to the possible rearrangement of the porosity field, i.e., the fluid escaping the medium).

With reference to Figure 2.1, the length of the interface Σ between the trabecular meshwork and the anterior chamber is $5.7 \cdot 10^{-4}$ [m], and the length of the separation between the trabecular meshwork and angular aqueous plexus ($\Gamma^{\rm out}$) is $3.4 \cdot 10^{-4}$ [m]. A parabolic profile for inlet velocity with a pulsating magnitude $u_{\rm in} = 4.89 \cdot 10^{-7} \sin^2(\pi t)$ [m $\cdot$ s^{-1}] (that has approximately the same frequency as the heart-beat) is imposed on $\Gamma^{\rm in}$ (the magnitude is obtained from the ratio $\frac{C\mu_s\kappa}{L\mu_f}$ with $C = 0.2$ integrated through the thickness and the condition is imposed through a Nitsche approach with penalty parameter equal to 1 since the relevant sub-boundary is not aligned with the axes), no-slip conditions are prescribed essentially on the walls, and a slip condition is considered for the fluid velocity on the symmetry axis (also imposed essentially). On the outlet $\Gamma^{\rm out}$ we impose zero fluid pressure $p_P = p_0$. We simulate the interfacial flow until $t = 5$ [s] and use a time step of $\Delta t = 0.1$ [s]. In this case, Taylor-Hood elements are used for the pairs [velocity, fluid pressure] and [displacement, total pressure], alongside continuous and piecewise quadratic elements for Biot fluid pressure. Figure 6.5 depicts the numerical solutions at two time instants, showing the distribution on the meridional axisymmetric domain of displacement, pressures and velocity (including the Darcy velocity in the trabecular meshwork) and illustrating the modification of flow patterns throughout the last cycle of the computation, and using (for this first run of simulations), a constant permeability $\kappa_0 = 5.0 \cdot 10^{-12}$ [m^2]. For sake of visualisation, we have also plotted the fluid pressure on both sub-domains rotationally extruded to a cut of the 3D domain.

In addition, we compare the behaviour produced by four heterogeneous permeability profiles (2.4). The first case has a gradient going from $\kappa_1^{\rm max} = 2.88 \cdot 10^{-11}$ [m^2] on the interface, linearly down to $\kappa^{\rm min} = 10^{-14}$ [m^2] on the outlet. A second synthetic permeability profile will decrease from the value $\kappa_2^{\rm max} = 6.55 \cdot 10^{-11}$ [m^2] on the interface down to $\kappa^{\rm min}$ on the outlet. These two profiles are generated by solving a Laplace problem with mixed boundary conditions, setting $\kappa_i^{\rm max}$ and $\kappa^{\rm min}$ essentially, and no-flux naturally on the remainder of Γ_P. A third permeability distribution is generated by a uniform random distribution bounded by $\kappa^{\rm min}$ and $\kappa_3^{\rm max} = 3.99 \cdot 10^{-11}$ [m^2], and a fourth case is constructed by placing random points in Ω_P having permeability $\kappa^{\rm min}$, and $\kappa_4^{\rm max} = 2.28 \cdot 10^{-11}$ [m^2] elsewhere (see the top panels of Figure 6.6). The maximum values $\kappa_i^{\rm max}$ were tuned so that the average permeability $\bar{\kappa}_i = \frac{1}{|\Omega_P|} \int_{\Omega_P} \kappa_i(r,z) {\rm d}r\,{\rm d}z$ is equal to $2.0 \cdot 10^{-11}$ in all four cases.

The effect of spatial variations in permeability are evaluated by imposing an inlet velocity profile (that is, equivalently, controlling the flow) with $\boldsymbol{u}_{\rm in} \cdot \boldsymbol{n} = -0.1t$ [m $\cdot$ s^{-1}] while prescribing zero fluid Biot pressure on $\Gamma^{\rm out}$. From the third row of Figure 6.6 we see that the pressure difference (intra-ocular fluid pressure minus the pressure at the angular aqueous plexus) remains roughly the same in all the cases consistently with the fact that $\bar{\kappa}$ is kept constant. Nonetheless we see that different permeability profiles give rise to slightly different spatial distributions for velocity, for the Biot fluid pressure, and for the strain (post-processed from the Biot displacement and from the harmonic extension Stokes displacement). Compared with the constant permeability case, that is the underlying field in the fourth permeability profile (right column), where the pressure decays linearly toward the outlet, in the decreasing permeability case (left column), the pressure gradient looks larger close to the inlet while the strain are, in general everywhere, lower; for the increasing permeability case (centre-left column) the pressure gradient is larger at the inlet and the strain are, in general everywhere, larger. Taking into consideration that here we investigate a much complex geometry, these speculations are consistent with the description provided in [50] and obtained in the limit of a slender geometry. The description provided here allows to speculate that a rearrangement of the microstructure could not

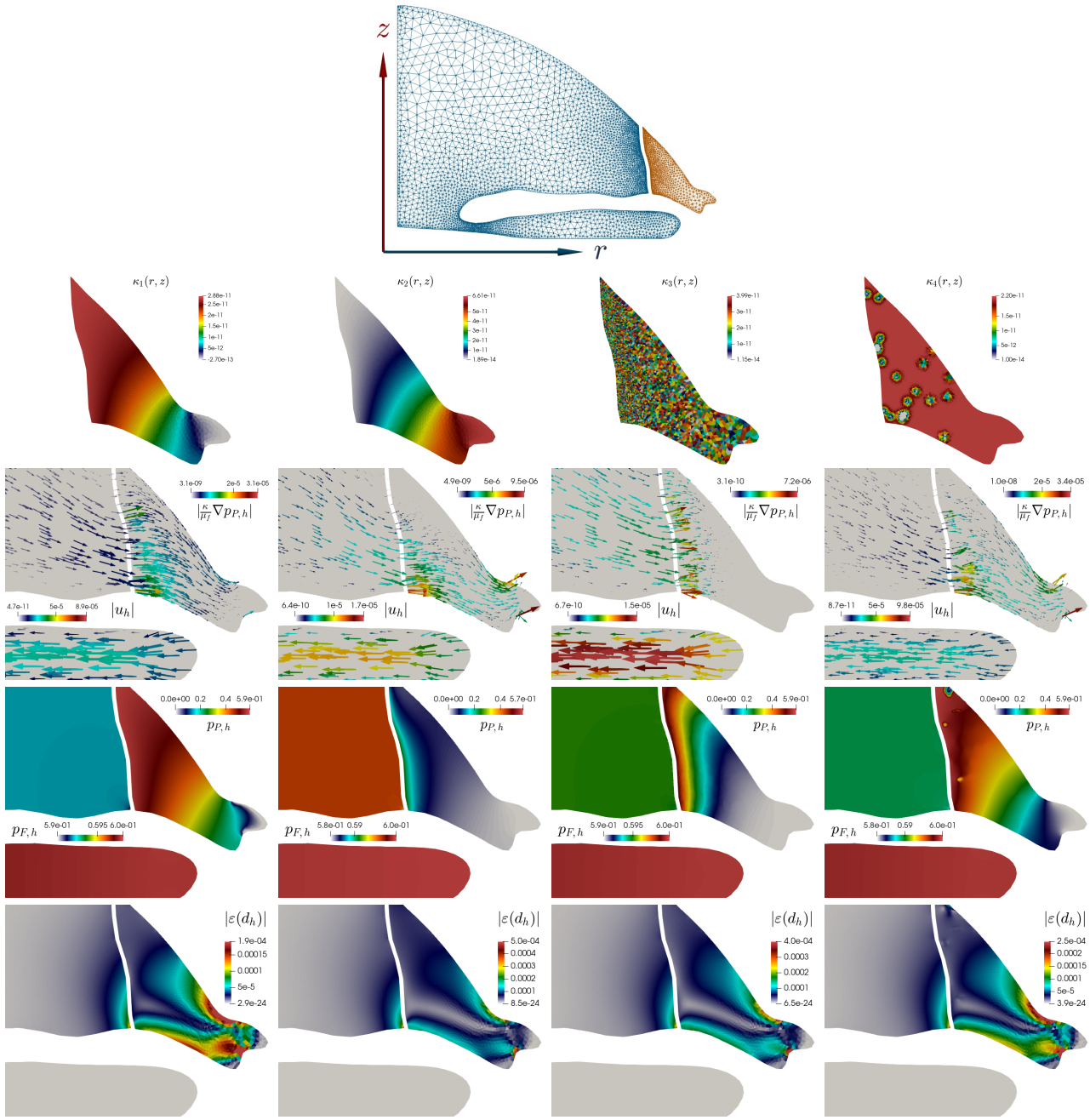

Figure 6.6: Example 4. Axisymmetric interfacial flow in the eye. Top: Coarse unstructured mesh indicating the axis of symmetry. Second row: four permeability distributions (in $[m^2]$) projected on piecewise constants over Ω_P. Linearly decreasing (left), linearly increasing (centre-left), with a log-random distribution (centre-right), and with randomly distributed spots of smaller permeability (right). In all cases the average permeability is $\bar{\kappa} = 2.0 \cdot 10^{-11}$. Third-fifth rows: comparisons of resulting profiles (velocity vectors, fluid pressure, and post-processed strain) at $t = 6$ [s].

drive a macroscopic change in the mechanics of the system within a short time horizon, since the flow and the pressure drop remains of the same order of magnitude; however, higher pressure and strain gradients could be the cause of a local remodelling of the tissue that, in the long term and in the nonlinear regime, could lead to a collapse of part of the pectinate ligaments.

7. Concluding remarks

We have introduced a new formulation for the coupling of Biot's poroelasticity system using total pressure and free flow described by the Stokes and Navier-Stokes equations, and which does not require Lagrange multipliers to set up the interface conditions between the two subdomains. The well-posedness of the continuous problem has been proved, we have provided a rigorous stability analysis. A mixed finite element method is defined for the proposed formulation together with a corresponding reduction to the axisymmetric case and the proposed schemes are robust with respect to the first Lamé parameter. We have conducted the numerical validation of spatio-temporal accuracy and have also performed some tests of applicative relevance, studying the behaviour of poromechanical filtration in subsurface hydraulic fracture with challenging heterogeneous material parameters, and simulating interfacial flow through the trabecular meshwork of the eye.

Different formulations we will study next include conservative discretisations on both poroelasticity and free flow [13, 34, 38]. We are currently working towards the design of monolithic block preconditioners being robust with respect to all material parameters, and whose construction hinges on adequate weighted Sobolev spaces and fractional interfacial norms. On the other hand, a crucial model extension corresponds to the regime of large deformations and the incorporation of remodelling mechanisms that would better explain the progressive consolidation of the interface and the shrinkage of the trabecular meshwork and associated ciliary cleft collapse seen in canines with glaucoma (using formalisms sharing similarities with the study of lamina cribrosa thickening [31]). There, it is also necessary to consider nonlinear variations on permeability depending on porosity, which in turn undergoes changes due to microstructural rearrangement [41].

Acknowledgments

This work has been partially supported by the Monash Mathematics Research Fund S05802-3951284; by the Ministry of Science and Higher Education of the Russian Federation within the framework of state support for the creation and development of World-Class Research Centers "Digital biodesign and personalised healthcare" No. 075-15-2020-926; by Gruppo Nazionale di Fisica Matematica (GNFM) of the Istituto Nazionale di Alta Matematica (INdAM); by a grant from the American College of Veterinary Ophthalmologists Vision for Animals Foundation VAFGL2017; and by NSF grant DMS 1818775. In addition, the authors gratefully acknowledge the many fruitful discussions with Wietse Boon, Elfriede Friedmann, Miroslav Kuchta, Kent-André Mardal, and Sarah L. Waters, regarding models and suitable discretisations for interfacial flow couplings.

References

[1] J. E. Aarnes, T. Gimse, and K.-A. Lie, *An introduction to the numerics of flow in porous media using Matlab*, in Geometric Modelling, Numerical Simulation, and Optimization: Applied Mathematics at SINTEF, G. Hasle, K.-A. Lie, and E. Quak, eds., Springer Berlin Heidelberg, Berlin, Heidelberg, 2007, pp. 265–306.

[2] C. Ager, B. Schott, M. Winter, and W. A. Wall, *A Nitsche-based cut finite element method for the coupling of incompressible fluid flow with poroelasticity*, Computer Methods in Applied Mechanics and Engineering, 351 (2019), pp. 253–280.

[3] M. Aletti, J.-F. Gerbeau, and D. Lombardi, *Modeling autoregulation in three-dimensional simulations of retinal hemodynamics*, Journal for Modeling in Ophthalmology, 1 (2016), pp. 88–115.

[4] M. S. Alnæs, J. Blechta, J. Hake, A. Johansson, B. Kehlet, A. Logg, C. Richardson, J. Ring, M. E. Rognes, and G. N. Wells, *The FEniCS project version 1.5*, Archive of Numerical Software, 3 (2015), pp. 9–23.

[5] I. Ambartsumyan, V. J. Ervin, T. Nguyen, and I. Yotov, *A nonlinear Stokes-Biot model for the interaction of a non-Newtonian fluid with poroelastic media*, ESAIM: Mathematical Modelling and Numerical Analysis, 53 (2019), pp. 1915–1955.

[6] I. Ambartsumyan, E. Khattatov, T. Nguyen, and I. Yotov, *Flow and transport in fractured poroelastic media*, GEM - International Journal on Geomathematics, 10 (2019), p. e11.

[7] I. Ambartsumyan, E. Khattatov, I. Yotov, and P. Zunino, *A Lagrange multiplier method for a Stokes–Biot fluid–poroelastic structure interaction model*, Numerische Mathematik, 140 (2018), pp. 513–553.

[8] V. Anaya, D. Mora, C. Reales, and R. Ruiz-Baier, *A vorticity-pressure finite element formulation for the Brinkman-Darcy coupled problem*, Numerical Methods for Partial Differential Equations, 35 (2019), pp. 528–544.

[9] S. Badia, A. Quaini, and A. Quarteroni, *Coupling Biot and Navier-Stokes equations for modelling fluid-poroelastic media interaction*, Journal of Computational Physics, 228 (2009), pp. 7986–8014.

[10] F. Ballarin, *multiphenics – easy prototyping of multiphysics problems in FEniCS*. https://mathlab.sissa.it/multiphenics. Accessed: 2020-03-11.

[11] P. G. Bedford and I. Grierson, *Aqueous drainage in the dog*, Research in Veterinary Science, 41 (1986), pp. 172–186.

[12] D. Boffi, F. Brezzi, and M. Fortin, *Mixed finite element methods and applications*, vol. 44, Springer, 2013.

[13] W. Boon, M. Kuchta, K.-A. Mardal, and R. Ruiz-Baier, *Robust preconditioners and stability analysis for perturbed saddle-point problems – application to conservative discretizations of Biot's equations utilizing total pressure*, SIAM Journal on Scientific Computing, 43 (2021), pp. B961–B983.

[14] J. H. Bramble, J. E. Pasciak, and O. Steinbach, *On the stability of the L^2 projection in $H^1(\Omega)$*, Mathematics of Computation, 71 (2002), pp. 147–156.

[15] K. E. Brenan, S. L. Campbell, and L. R. Petzold, *Numerical solution of initial-value problems in differential-algebraic equations*, SIAM, 1995.

[16] M. Bukač, I. Yotov, R. Zakerzadeh, and P. Zunino, *Partitioning strategies for the interaction of a fluid with a poroelastic material based on a Nitsche's coupling approach*, Computer Methods in Applied Mechanics and Engineering, 292 (2015), pp. 138–170.

[17] M. Bukač, I. Yotov, and P. Zunino, *An operator splitting approach for the interaction between a fluid and a multilayered poroelastic structure*, Numerical Methods for Partial Differential Equations, 31 (2015), pp. 1054–1100.

[18] S. A. Cannizzo, G. A. Lewbart, and H. D. Westermeyer, *Intraocular pressure in American Bullfrogs (Rana catesbeiana) measured with rebound and applanation tonometry*, Veterinary Ophthalmology, 20 (2017), pp. 526–532.

[19] A. Cesmelioglu, *Analysis of the coupled Navier–Stokes/Biot problem*, Journal of Mathematical Analysis and Applications, 456 (2017), pp. 970–991.

[20] A. Cesmelioglu and P. Chidyagwai, *Numerical analysis of the coupling of free fluid with a poroelastic material*, Numerical Methods for Partial Differential Equations, 36 (2020), pp. 463–494.

[21] M. A. Christie and M. Blunt, *Tenth SPE comparative solution project: A comparison of upscaling techniques*, SPE Reservoir Evaluation & Engineering, 4 (2001), pp. 308–317.

[22] P. G. Ciarlet, *The finite element method for elliptic problems*, SIAM, 2002.

[23] O. Coussy, *Poromechanics*, John Wiley & Sons Ltd, Chichester, UK, 2004.

[24] S. C. Cowin and S. B. Doty, *Tissue Mechanics*, Springer-Verlag, New York, USA, 2007.

[25] T. R. Crowder and V. J. Ervin, *Numerical simulations of fluid pressure in the human eye*, Applied Mathematics and Computation, 219 (2013), pp. 11119–11133.

[26] M. Dalwadi, S. J. Chapman, S. L. Waters, and J. Oliver, *On the boundary layer structure near a highly permeable porous interface*, Journal of Fluid Mechanics, 798 (2016), pp. 88–139.

[27] L. M. De Oliveira Vilaca, B. Gómez-Vargas, S. Kumar, R. Ruiz-Baier, and N. Verma, *Stability analysis for a new model of multi-species convection-diffusion-reaction in poroelastic tissue*, Applied Mathematical Modelling, 84 (2020), pp. 425–446.

[28] J. A. Ferreira, P. de Oliveira, P. M. da Silva, and J. N. Murta, *Numerical simulation of aqueous humor flow: From healthy to pathologic situations*, Applied Mathematics and Computation, 226 (2014), pp. 777–792.

[29] A. D. Fitt and G. Gonzalez, *Fluid mechanics of the human eye: Aqueous humour flow in the anterior chamber*, Bulletin of Mathematical Biology, 68 (2006), p. 53.

[30] A. Gizzi, M. L. D. Bellis, M. Vasta, and A. Pandolfi, *Diffusion-based degeneration of the collagen reinforcement in the pathologic human cornea*, Journal of Engineering Mathematics, 127 (2021), p. 3.

[31] R. Grytz, I. A. Sigal, J. W. Ruberti, G. Meschke, and J. C. Downs, *Lamina cribrosa thickening in early glaucoma predicted by a microstructure motivated growth and remodeling approach*, Mechanics of Materials, 44 (2012), pp. 99–109.

[32] G. G. Gum, K. N. Gelatt, and D. Esson, *Physiology of the Eye*, In: Veterinary Ophthalmology 4th edition (ed.: K. N. Gelatt), (2007), pp. 149–182.

[33] J. J. Heys, V. H. Barocas, and M. J. Taravella, *Modeling passive mechanical interaction between aqueous humor and iris*, Journal of Biomechanical Engineering, 123 (2001), pp. 540–547.

[34] Q. Hong, J. Kraus, M. Lymbery, and F. Philo, *A new framework for the stability analysis of perturbed saddle-point problems and applications in poromechanics*, arXiv preprint 2103.09357, (2021).

[35] M. A. Johnstone, *The aqueous outflow system as a mechanical pump: Evidence from examination of tissue and aqueous movement in human and non-human primates*, Journal of Glaucoma, 13 (2004), pp. 421–438.

[36] T. Karper, K.-A. Mardal, and R. Winther, *Unified finite element discretizations of coupled Darcy–Stokes flow*, Numerical Methods for Partial Differential Equations, 25 (2009), pp. 311–326.

[37] S. Kumar, S. Acharya, R. Beuerman, and A. Palkama, *Numerical solution of ocular fluid dynamics in a rabbit eye: parametric effects*, Annals of Biomedical Engineering, 34 (2006), pp. 530–544.

[38] S. Kumar, R. Oyarzúa, R. Ruiz-Baier, and R. Sandilya, *Conservative discontinuous finite volume and mixed schemes for a new four-field formulation in poroelasticity*, ESAIM: Mathematical Modelling and Numerical Analysis, 54 (2020), pp. 273–299.

[39] H. Kunwar, H. Lee, and K. Seelman, *Second-order time discretization for a coupled quasi-Newtonian fluid-poroelastic system*, International Journal for Numerical Methods in Fluids, 92 (2020), pp. 687–702.

[40] J. Lee, K.-A. Mardal, and R. Winther, *Parameter-robust discretization and preconditioning of Biot's consolidation model*, SIAM Journal on Scientific Computing, 39 (2017), pp. A1–A24.

[41] C. W. MacMinn, E. R. Dufresne, and J. S. Wettlaufer, *Large deformations of a soft porous material*, Physical Review Applied, 5 (2016), p. 044020.

[42] G. J. Martinez Sánchez, C. E. del Pozo, and J. A. R. Medina, *Numerical model of aqueous humor drainage: effects of collector channel position*, Medical Engineering & Physics, 65 (2019), pp. 24–30.

[43] J. M. Meekins, A. J. Rankin, and D. A. Samuelson, *Ophthalmic Anatomy*, in Veterinary Ophthalmology: Volume I. Sixth Edition, K. N. Gelatt, G. Ben-Shlomo, B. C. Gilger, D. V. Hendrix, T. J. Kern, and C. E. Plummer, eds., John Wiley & Sons Inc., US, 2021, ch. 2, pp. 41–121.

[44] M. A. Murad, J. N. Guerreiro, and A. F. D. Loula, *Micromechanical computational modeling of secondary consolidation and hereditary creep in soils*, Computer Methods in Applied Mechanics and Engineering, 190 (2001), pp. 1985–2016.

[45] R. Oyarzúa and R. Ruiz-Baier, *Locking-free finite element methods for poroelasticity*, SIAM Journal on Numerical Analysis, 54 (2016), pp. 2951–2973.

[46] R. Pearl, D. Gould, and B. M. Spiess, *Progression of pectinate ligament dysplasia over time in two populations of Flat-Coated Retrievers*, Veterinary Ophthalmology, 18 (2015), pp. 6–12.

[47] A. Quarteroni and A. Valli, *Numerical approximation of partial differential equations*, vol. 23, Springer Science & Business Media, 2008.

[48] L. R. Scott and S. Zhang, *Finite element interpolation of nonsmooth functions satisfying boundary conditions*, Math. Comput., 54 (1990), pp. 483–493.

[49] R. E. Showalter, *Poroelastic filtration coupled to Stokes flow*, in Control Theory of Partial Differential Equations, O. Imanuvilov, G. Leugering, R. Triggiani, and B.-Y. Zhang, eds., vol. 242 of Lecture Notes in Pure and Applied Mathematics, Chapman & Hall, Boca Raton, 2005, pp. 229–241.

[50] M. Taffetani, R. Ruiz-Baier, and S. L. Waters, *Coupling Stokes flow with inhomogeneous poroelasticity*, Quarterly Journal of Mechanics and Applied Mathematics, in press (2021).

[51] B. Tully and Y. Ventikos, *Coupling poroelasticity and CFD for cerebrospinal fluid hydrodynamics*, IEEE Transactions on Biomedical Engineering, 56 (2009), pp. 1644–1651.

[52] A. Villamarin, S. Roy, R. Hasballa, O. Vardoulis, P. Reymond, and N. Stergiopulos, *3D simulation of the aqueous flow in the human eye*, Medical Engineering & Physics, 34 (2012), pp. 1462–1470.

[53] S.-Y. Yi, *Convergence analysis of a new mixed finite element method for Biot's consolidation model*, Numerical Methods for Partial Differential Equations, 30 (2014), pp. 1189–1210.

[54] J. Zhang, X. Qian, H. Zhang, and Z. Liu, *Fluid-structure interaction simulation of aqueous outflow system in response to juxtacanalicular meshwork permeability changes with a two-way coupled method*, Computer Modeling in Engineering & Sciences, 116 (2018), pp. 301–314.